Janus Magnetic-Plasmonic Nanoparticles for Magnetically Guided and Thermally Activated Cancer Therapy

Ana Espinosa, Javier Reguera*, Alberto Curcio, Álvaro Muñoz-Noval, Christian Kuttner, Aurore Van de Walle, Luis M. Liz-Marzán and Claire Wilhelm*

Dr. A. Espinosa, Dr. A. Curcio, Dr. Aurore Van de Walle, Prof. C. Wilhelm
Laboratoire Matière et Systèmes Complexes (MSC), UMR 7057, CNRS and Université Paris Diderot, 75205 Paris cedex 13, France

Dr. A. Espinosa
IMDEA Nanociencia, c/ Faraday, 9, 28049 Madrid, Spain
E-mail: ana.espinosa@imdea.org

Dr. J. Reguera, Dr. Christian Kuttner, Prof. L. M. Liz-Marzán
CIC biomaGUNE and Ciber-BBN, Paseo de Miramón 182, 20014 Donostia-San Sebastián, Spain and Ikerbasque, Basque Foundation for Science, 48013 Bilbao, Spain

Dr. J. Reguera
BCMaterials, Basque Center for Materials, Applications and Nanostructures, UPV/EHU Science Park, 48940 Leioa, Spain
E-mail: javier.reguera@bcmaterials.net

Dr. A. Muñoz-Noval
Dpto. Física Materiales, Facultad CC. Físicas, Universidad Complutense de Madrid, 28040 Madrid, Spain

Keywords: magnetic-plasmonic nanohybrids, nano-heat, dual heating, magnetically-guided nanoparticles, magneto-photo-thermia

Progress of thermal tumor therapies and their translation into clinical practice are limited by insufficient nanoparticle concentration to release therapeutic heating at the tumor site after systemic administration. We propose herein the use of Janus magneto-plasmonic nanoparticles, made of gold nanostars and iron oxide nanospheres, as efficient therapeutic nanoheaters whose on-site delivery can be improved by magnetic targeting. Single and combined magneto- and photo-thermal heating properties of Janus nanoparticles render them as compelling heating elements, depending on the nanoparticle dose, magnetic lobe size and milieu conditions. In cancer cells, a much more effective effect was observed for photothermia compared to magnetic hyperthermia, while combination of the two modalities into a magneto-photo-thermal treatment

resulted in a synergistic cytotoxic effect *in vitro*. The high potential of the Janus nanoparticles for magnetic guiding confirmed them to be excellent nanostructures for *in vivo* magnetically-enhanced photothermal therapy, leading to efficient tumor growth inhibition.

1. Introduction

One of the main goals of nanomedicine is the development of efficient therapeutic and diagnostic tools that overcome the limitations of current treatments, through the use of inorganic nanostructures.[1] These nano-objects can overcome cellular and physiological barriers, target the entities of tumor environment and induce physical therapeutic effects after being stimulated by a remote signal, thereby enabling a site-specific treatment. Such strategies can prevent damage to surrounding healthy cells and limit the unwanted side effects of current treatments. However, although significant progress has been made in the transfer of nanotechnology to medicine, efforts are still needed to convert nanobiotechnology into a clinical reality.[2]

In this context, treatments based on the elevation of local temperature for therapeutic purposes enabled by heating-activatable nanomaterials, also called nanothermotherapies, have emerged as a promising biomedical strategy.[3] Magnetic field-induced hyperthermal cancer therapy (or magnetic hyperthermia, MHT) is based on the use of magnetic particles as heating mediators when subjected to an alternating magnetic field (AMF).[4] An alternative hyperthermal modality, photothermal therapy (PTT), is based on the activation of nanoparticles when illuminated with laser radiation in the near infrared region (NIR), where absorption by biological tissues is minimal.[5] PTT has been traditionally focused on the highly efficient heating properties of photothermal nanoparticles, typically gold- or carbon-based.[6] MHT and PTT have evolved independently as two distinct therapeutic disciplines, and they have only recently been compared, identifying different windows of applicability.[7]

From a theranostics perspective, the magnetic and plasmonic association has garnered particular attention over the past few years due to its multifunctional potential for biomedical applications.

Indeed, besides MHT, the magnetic part offers other functions such as contrast for magnetic resonance imaging (MRI) or magnetic-based targeting and drug delivery.[8] The plasmonic part endows the optical sensing ability to nanostructures to develop building blocks devices such as biosensors imaging agents[9] and nanophotonic entities.[10] Magneto-plasmonic hybrids thus combine complementary theranostic strategies in a unique structure, including multimodal MRI-optical imaging-based systems;[11] optically-guided magnetic separation;[12] MRI-guided gold-based photothermal therapy;[13] or stimuli-responsive drug delivery in dual- or multi-functional action with magnetic and plasmonic features.[14] In this rapidly expanding domain, the combination of the two thermal modalities altogether (dual-action MHT and PTT) in one-single magneto-plasmonic object[15] has been recently established as another appropriate and efficient thermal modality in cancer nanotechnology. Several studies based on nanoparticles made of an iron oxide core and a plasmonic shell (gold or silver) have demonstrated such efficiency (see **Table S1**). Besides, magnetic nanoparticles were recently found to be valuable PTT agents in the NIR, on top of their intrinsic heating potential for MHT,[16] which also allowed to combine both modalities in magneto-photo-thermal tumor treatment.[17] However, the association of magnetic guiding and PTT have thus far attracted less attention and has been only scarcely investigated in magneto-plasmonic nanohybrids,[14a, 18] with just a few works reporting *in vivo* results (see **Table S2**). Among them, Huang et al.[18a] recently showed efficient tumor eradication using magnetic homing of gold/iron oxide nanocapsules associated with 1 W/cm^2-PTT ablation and anticancer drug delivery. Furthermore, the combination of magnetically-guided targeting and subsequent 1.3 W/cm^2-PTT irradiation of gold and iron multi-shells resulted in high therapeutic efficacy.[14a] In both studies, the treatments were complemented with the locally delivery of drugs. Yang et al.[18c] combined dual MRI/photoacoustic (PA) imaging with magnetically guided high-dose PTT (2 W/cm^2) employing magnetic polymer-modified gold nanorods in a 10-days period treatment.

With regard to the nanosystem layout, different hybrid magneto-plasmonic configurations based on gold and iron oxide including core/shell,[13i, 19] heterodimer and dumbbell structures,[20] core-satellite,[21] and nanoclusters[12a, 22] have been designed for biomedical purposes. Among the broad range of possible architectures, Janus nanoparticles have attracted increased scientific interest in the technological and biomedical fields.[23] They possess an anisotropic structure with two chemically distinct faces that provide them with unique properties such as nano-amphiphilicity, or binary asymmetric biofunctionalization. Their simple anisotropic features make them interesting in a wide set of applications, including Pickering emulsions for nanoreactors, nanojets and nanomotors, enhanced catalysts, or just as building blocks for more complex supracrystals and molecular colloids.[24] Among biomedical applications, Janus nanoparticles have been proposed for cell-membrane penetration[25], biosensing[26], or nanozymes[27], but they can also be used for further straightforward selective biofunctionalization. From the possible Janus component nanoparticles, those made of gold and iron oxide have been proven as efficient theranostic platforms for multimodal imaging with enhanced resolution and sensitivity and a versatile multifunctionalization. Recently, Janus nanoparticles made of epitaxially-bound gold nanostars and iron oxide nanospheres were reported as efficient magnetically-manipulated probes for surface-enhanced Raman spectroscopy (SERS)[28] and for tri-modal imaging,[13c, 29] (computed tomography (CT)-magnetic resonance (MRI)-photoacoustic (PA)) exhibiting a strong plasmonic response in the NIR, provided by the gold-based branched structures, which can be tuned by adjusting the tips aspect ratio.[30] These gold-branched partial shells were based on state-of-the-art gold nanostars[30-31], instead of other types of gold morphologies, because of their ease of synthesis, which is independent of the Au seed in heterodimers, their excellent photothermal efficiency, and the lack of toxic compounds such as Ag or cetyltrimethyl ammonium bromide (CTAB) as shape directing agents present on other gold morphologies.[32]

All magneto-plasmonic configurations assessed for combined bimodal MHT and PTT or for magnetically-guided PTT are based on either a core-shell or a multi-shell structure (see summary in Tables S1 and S2), whereas the Janus iron oxide-gold architecture has not been investigated, despite its promising potential. More specifically, Janus nanoparticles composed of an iron oxide nanosphere and a gold nanostar have not been evaluated, despite the high photothermal capability of gold nanostars.[13c, 33] Additionally, the magnetic features of iron oxide nanospheres can be used for *in vivo* targeting, offering the prospect of guiding the nanoparticles at the tumor site and increasing treatment efficiency.

In this study, Janus nanoparticles composed of an iron oxide nanosphere and a gold nanostar were thus considered for both photo-magneto-thermal activation and magnetic guidance. Magnetic hyperthermia (MHT) and photothermal therapy (PTT) were compared in terms of thermal efficiency relative to the nanoparticles dose, iron/gold ratio, and magnetic core size. The dual magneto-photothermal modality was also assessed. We demonstrate that our Janus nanoparticles are not only good nanoheaters for hyperthermia but also (and mostly) for photothermia. Magnetic guidance of nanoparticles was evaluated *in vitro* and *in vivo*, and associated with PTT for synergistically enhanced therapy. Upon magnetic intratumoral accumulation, photothermal tumor therapy enabled tumor treatment after 1-day shot exposure at moderate laser power (0.8 W/cm^2, 680 nm). This *in vivo* magnetically-guided targeting added to photothermal treatment remarkably reduced tumor growth.

2. Results and discussion

2.1. Tunable synthesis of Janus nanoparticles, with controlled magnetic core size of 16 and 20 nm and growth of optimized gold tips

Janus nanoparticles were synthesized using two seed-mediated synthesis steps (see experimental section). [28-29] Briefly, gold-iron oxide heterodimers were first synthesized in one pot by formation of gold nanoparticles (d ~ 6 nm) and subsequent growth of iron oxide.[20a] The branched gold structure was grown from the gold lobe of the heterodimer seeds, using the polyvinylpyrrolidone/dimethylformamide (PVP/DMF) nanostar synthesis route and maintaining the initial Janus structure.[30, 34] The relative size of the two parts can be easily tuned by adjusting the seeds/precursor ratio, and the final nanoparticles are coated with PVP. This polymer coating provides stability in water, as well as further selective functionalization by ligand exchange of weakly bound PVP by ligands with higher-affinity chemical groups (for instance thiols for the gold surface, and catechols, silanes, or phosphonates for the iron oxide surface).

Figure 1A shows representative transmission electron microscopy (TEM) images of two Janus nanoparticle samples, with different sizes. They were chosen to display a small size, with low Au:Fe ratio, while maintaining a plasmonic absorption in the red and NIR range of the spectrum (first transparency window). The iron oxide lobe size (16.2 ± 2.8 nm or 20.5 ± 4.0 nm) was adjusted by changing the Au:Fe ratio in the initial heterodimer formation process. The size of the nanostar was then tuned by varying the amount of heterodimer seeds to a growth solution containing chloroauric acid and PVP in DMF (see Experimental Section). The nanoparticles were denoted Fe(16)@Au (d_{MAG} = 16 nm) and Fe(20)@Au (d_{MAG} = 20 nm), with overall equivalent diameters of 28.5 ± 2.9 nm and 35.8 ± 5.0 nm, respectively, as measured by TEM and assuming a spherical shape (see size distribution histograms in **Figure S1** and summary in **Table S3**). Both particles have relatively similar molar gold to iron ratios of [Au]/[Fe] = 1.6 and 2.3, respectively (calculated from inductively coupled plasma mass spectroscopy, ICP-MS).

The high content in Au is needed to ensure the star-like branched architecture for photothermal heating. The magnetic part was also optimized to maintain their superparamagnetic properties with high saturation magnetization, in order to elicit the magnetic hyperthermia and magnetic guided targeting applications. Indeed, both demand a significant dose of magnetic nanoparticles, e.g. 5-15 mg/kg of Fe for magnetic drug delivery applications.[35]

The two synthesized Janus nanoparticles displayed localized surface plasmon resonances (LSPR) in the Vis-NIR region (Figure 1B), with a small band due to a dipolar plasmon mode localized in the nanoparticle core at the 500-600 nm region, and a more intense band in the 600-800 nm region attributed to a tips-core hybridized plasmon mode.[30] As the nanoparticle size is increased (from 16 to 20 nm for the iron oxide diameter), the number and length of embracing gold spikes is incremented and the LSPR maximum shifts accordingly toward the NIR region (from 600 nm for Fe(16)@Au to 680 nm for Fe(20)@Au). Energy-dispersive X-ray spectroscopy (EDX) mapping illustrates the anisotropic structure of the Janus nanoparticles and shows the two chemically distinct domains, corresponding to the Fe and Au atoms, in close contact and forming a two-phase structure (Figure 1C). Electromagnetic simulations predict that for Janus nanostars, light absorption is strongly dominant over light scattering (**Figure S2** and **Figure S3**). By performing diffuse reflectance spectroscopy measurements [36], we could experimentally confirm the simulations (**Figure S4** and **Figure S5**). In fact, we found that at 680 nm, regardless of the size of the iron oxide core, approx. 90% of light is absorbed and thus qualifying such Janus nanoparticles as highly efficient photothermal heaters [37]. Characterization of the Janus nanoparticles using X-ray absorption spectroscopy (XAS) at the Au-L_3 edge is shown in **Figure S6**. The X-ray absorption near-edge structure (XANES) confirmed the existence of a metallic Au-rich branched-shell bonded to the iron oxide core in both nanoparticles (same energy edge as for bulk Au metal). The Fourier transform (FT) of the extended X-ray absorption fine structure (EXAFS) oscillation of the Janus nanoparticles and bulk Au reference (without phase correction) exhibited two peaks that correspond to the first

coordination shell of metallic Au (Au-Au = 2.86 Å, coordination number = 12).[38] Listed in **Table S4** are the obtained EXAFS fitting parameters, which are further summarized in Figure S6. The decrease in the magnitude of the FT peaks in both Janus particles, relative to the gold foil, is ascribed to the inherently small length scale (nanometer range) of Janus nanoparticles compared to bulk foil, as can be quantitatively observed in the average number of atomic neighbors obtained by EXAFS (Table S4) for the nanoparticles (N = 11 ± 1) compared to bulk (N =12 ± 1)). The iron oxide part corresponds to a magnetite crystalline nanosphere (Fe_3O_4) as determined by X-ray photoelectron spectroscopy (XPS) analysis.[29] It is known that magnetite-based iron oxide nanoparticles exhibit optical absorbance in the NIR[17], however, in dilute samples the absorption is much less effective than that attributable to LSPR (Figure S2B).[7] X-ray diffraction (XRD) patterns also confirmed the presence of iron oxide spinel structures as well as metallic gold crystalline phases (see **Figure S7**A), and scanning electron microscopy (SEM) revealed the spiked morphology of the Janus nanoparticles (Figure S7B).

Regarding their magnetic properties, both Janus nanoparticles yield a superparamagnetic response at room temperature (see **Figure S8**), maintaining their magnetic behavior after growth of the gold branches, with saturation magnetization Ms = 74-77 emu/g (see Table S3).

2.2. Magneto- and photo-thermal heating capacities of Janus nanoparticles

Magneto- and photo-thermal efficiency of Fe(20)@Au and Fe(16)@Au Janus nanoparticles was evaluated in aqueous dispersions using three protocols (**Figure 2**). First, the nanoparticles were subjected to an alternating magnetic field at 470 kHz and 18 mT to assess their magneto-thermal heating (MHT). The nanoparticles were then irradiated with a laser at 680 nm and 0.5 W/cm^2 to measure photo-thermal heating (PTT). Finally, both thermal stimuli were applied simultaneously (DUAL, MHT + PTT).

For Fe(20)@Au, the temperature increments ΔT reached under MHT, PTT and DUAL after 5 minutes of treatment are displayed in Figure 2A. This temperature was assessed for Fe concentrations ranging from 0.05 to 24 mM and measured using an infrared thermographic

camera; typical infrared thermal images are shown in Figure 2B. Temperature elevation via magnetic hyperthermia (MHT) was only detected for concentrations superior or equal to 3 mM and was linear from 3 to 24 mM, reaching 5 °C as maximum temperature increment. For photothermia (PTT), two regimes were observed: i) at low concentrations (0.05 to 3 mM) the heating linearly increases up to ii) reaching saturation at high concentrations (≥ 6 mM), due to limited laser penetration (ΔT ~ 28 °C). PTT is undoubtedly more effective than MHT at low doses, and MHT becomes competitive with PTT only at high doses of material. This marked difference in the concentration range of applicability is also evidenced by the DUAL mode, which is only improved compared to single-PTT modality at high doses. At [Fe] = 24 mM, the heating efficiency is amplified by about 20 % compared to PTT: heating increases from ΔT ~ 28 °C to 34 °C.

The heating efficiency (or specific absorption rate, SAR, see Experimental section for description) of the material was then calculated by measuring the initial slope of the temperature increase versus time (where thermal losses can be neglected) and normalized to the total amount of material (Fe_3O_4 and Au content) (Figure 2C). Results show that MHT heating capability remains constant at increasing concentrations, with values around 15 $W/g_{Fe3O4+Au}$, which corresponds to 140 W/g_{Fe} if only the iron mass is considered. This SAR value, expressed per mass of iron, is competitive within the MHT field. It can be compared for instance with iron oxide nanocubes, which are some of the best MHT nanoheaters, with SAR values around 400 W/g_{Fe} in the same experimental parameters setting.[7] For PTT, two regimes were observed with a first linear increase in heating at low concentrations, and a very efficient photothermal effect, with remarkably high SAR values (e.g. 18 $kW/g_{Fe3O4+Au}$ at [Fe] = 0.05 mM). At high concentrations, the heating capacity saturates due to limited laser penetration (ΔT ~ 28 °C). As a result, SAR decreases (e.g. 199 $W/g_{Fe3O4+Au}$ at [Fe] = 12 mM falling to 104 $W/g_{Fe3O4+Au}$ at [Fe] = 24 mM). The heating transfer of nanoparticles produced by PTT is then strongly

dependent of nanoparticle concentration, where light absorption of laser intensity increases with concentration according to the Beer–Lambert law (see Experimental section). At high concentration, the heating then saturates, and increasing the concentration is not anymore beneficial to heat generation. In the DUAL mode, the interesting contribution of MHT at high concentrations only is also observed, with the SAR increasing from 104 to 130 kW/ $g_{Fe3O4+Au}$ at [Fe] = 24 mM when compared to the single-PTT modality.

Figures 2D and 2E focus on the heating effect of Fe(16)@Au nanoparticles, for Fe concentrations ranging from 12 to 48 mM. At first sight, it appears that the MHT outcome is higher than for Fe(20)@Au. For instance, at [Fe] = 24 mM, the temperature elevation generated by Fe(16)@Au ($\Delta T \sim 10$ °C) is amplified 2-fold compared to Fe(20)@Au and the SAR is 26 $W/g_{Fe3O4+Au}$ (245 W/g_{Fe}). This is in agreement with previous experimental and theoretical studies, which reported an optimal magnetic heating performance for a diameter of 12-16 nm in iron oxide nanoparticles.[39] Besides, a SAR value of 245 W/g_{Fe} is highly competitive for the MHT field. However, concerning PTT with Fe(16)@Au, temperature increments and SAR values are lower than the ones obtained with Fe(20)@Au (e.g. $\Delta T \sim 10$ °C, 150 $W/g_{Fe3O4+Au}$ at [Fe] = 12 mM; $\Delta T \sim 16$ °C, 98 $W/g_{Fe3O4+Au}$ at [Fe] = 24 mM). This is due to the lower absolute absorption at the selected 680-nm irradiation wavelength (see UV-Vis-IR spectra in Figure 1). As a result, for Fe(16)@Au, the DUAL modality is more relevant, with an increase of 14, 18 and 40 % compared to PTT stand-alone treatment, at [Fe] = 12 mM (174 $W/g_{Fe3O4+Au}$), [Fe] = 24 mM (120 $W/g_{Fe3O4+Au}$), and [Fe] = 48 mM (70 $W/g_{Fe3O4+Au}$), respectively.

The above values were compared with the photothermal heating efficiency of standard gold nanostars of similar size (25 nm), which also yielded a maximum absorbance around 700 nm.[7, 31] For these nanostars we obtained SAR values of 1.5 kW/g_{Au} at [Au] = 2.5 mM and 135 W/g_{Au} at [Au] = 30 mM (using a 680 nm laser at 0.5 W/cm²).[7] For comparison, we normalized the PTT SAR value of both Fe(16)@Au and Fe(20)@Au samples, at the same laser setting, only

by the Au content. For Fe(20)@Au, SAR is 0.7 kW/g_{Au} at [Au] = 2.6 mM, and for Fe(16)@Au, SAR value is 77 W/g_{Au} at [Au] = 30 mM, i.e. in the same order of those obtained for gold nanostars. Therefore, the windows of applicability of MHT and PTT have been defined for the first magnetic-plasmonic hybrids depending on the nanoparticle size, design and dispersion medium.

2.3. Impact of the cell environment on heat generation with Janus nanoparticles *in vitro*

The clinical development of any nanoparticle aiming at cancer treatment requires a complete understanding of their behavior when in contact with their targeted environment and in particular with cancer cells, into which they would eventually be internalized. Their physicochemical properties, such as magnetic- and photo-activated thermal capabilities can indeed be altered by the cellular environment. For instance, the confinement of magnetic nanoparticles inside cells and subsequent increase of dipole–dipole interactions, can significantly reduce their global magnetic heating response.[40] On the contrary, optical spectral shifting and broadening of metal nanoparticles aggregated in cells can be favorable to PTT in the near-infrared range.[31, 41] Both types of Janus nanoparticles, Fe(20)@Au and Fe(16)@Au, were incubated with CT-26 cancer cells for 24 hours at an extracellular iron concentration of [Fe] = 100 µM. **Figure 3**A illustrates the cellular uptake for Fe(20)@Au, by transmission electron microscopy (TEM) imaging, which clearly demonstrates the sequestration of the nanoparticles within endosomes (endocytosis-mediated pathway). For both Fe(16)@Au and Fe(20)@Au, the 24 hours incubation at [Fe] = 100 µM resulted in similar mass of iron uptaken by cell, of 2.9 ± 0.5 and 3.1 ± 0.6 pg of Fe per cell, for Fe(16)@Au and Fe(20)@Au, respectively. After incubation, cells were detached and suspended in small pellets with high cell density mimicking tumor cell assemblies. The goal was to reach similar concentrations in Fe as those previously investigated in water, and the cellular pellets were adjusted to reach exactly [Fe] = 6 mM, corresponding to approximately 6 million cells dispersed in 50 µL (see **Table 1** for exact cell density). Figure 3B and 3C show the heating of the corresponding cell samples, under MHT

and PTT respectively, which clearly illustrates that the MHT heating performance is much lower (ΔT ~ 1-2 °C) compared to PTT response (ΔT ~ 30 °C). Supplementary MHT and PTT data at additional incubation concentrations and the resulting internalized iron concentrations are presented in Table 1. The difference between MHT and PTT is striking, with PTT efficiency disproportionately higher than that for MHT. This difference is further evidenced by calculation of SAR values (Figure 3D and 3E, for MHT and PTT respectively), at 3-4 $W/g_{(Fe3O4+Au)}$ with MHT, for both nanoparticle types, increasing to 200-400 $W/g_{(Fe3O4+Au)}$ with PTT. It is important however to emphasize here again that these SAR values are expressed as W per total mass of nanoparticles (mass of Fe_3O_4+Au). If expressed in W per gram of Fe, the SARs of Fe(16)@Au and Fe(20)@Au, have values at 68 ± 6 and 53 ± 5 W/g_{Fe}, respectively. Besides, we must emphasize that, for the most efficient nanoparticles for MHT (e.g. magnetic nanocubes or magnetosomes), their SAR decreases, once in the cellular environment, below 100 W/g_{Fe} (88 W/g_{Fe} for magnetic nanocubes[7], and 60 W/g_{Fe} for magnetosomes[42], for the same magnetic field setting), therefore the both Janus nanoparticles still have significant cellular SAR values, respective to the MHT field. Representative infrared thermal images of the samples subjected to MHT and PTT are displayed in Figure 3F. Magnetization curves of nanoparticles in cells measured at 300 K are shown in **Figure S9**. For both nanoparticles (Fe(16)@Au and Fe(20)@Au) the magnetization saturation in cells yielded values similar to those in aqueous dispersion (71 ± 11 emu/g_{Fe} for Fe(16)@Au in cells and 68 ± 8 emu/g_{Fe} for Fe(20)@Au in cells) but slightly reduced initial susceptibility (see Figure S8 and S9B). The Janus nanoparticles remain thus competitive MHT agents in the cellular environment, even if the heating characterization in cancer cells unequivocally confirms a remarkable superiority of PTT as a thermal treatment.

The assessment of thermally-triggered death of cancer cells is shown in Figure 3G, which shows cells metabolic activity 24 hours after the different thermal treatments (MHT, PTT, and DUAL for 15 min) in CT-26 cells labeled with Fe(16)@Au. Results show that MHT did not impact

cell viability (~100%) compared to unlabeled cells used as controls, in agreement with the low magnetic heating response in cells (Figure 3B). On the other hand, PTT modality significantly affected cell viability, which dropped below 20%. Remarkably, the DUAL action yielded even higher heat-mediated cell mortality (3-4% surviving rate), despite the insignificant individual MHT outcome. DUAL (magneto-photo-thermal effect) application thus resulted in a synergistic efficacy rather than a combinatorial effect. The cooperative therapeutic exploitation of heat upon alternating magnetic field exposure and laser irradiation has been previously reported, exhibiting a symbiotic efficiency using iron oxide-based nanoparticles (Fe_3O_4, $MnFe_2O_4$, and Fe_2O_3-CuS) on cell death, despite the low heating performance of MHT in cells.[17, 43] Herein, the imperceptible initial MHT input in cells turned into an efficient therapeutic adjuvant partner for PTT. This result confirms the ability of MHT to produce local effects in the absence of a macroscopic temperature increase, also exploited to enhance drug cytotoxicity by MHT-mediated local nanoscale heating.[44]

2.4. Magnetic guiding potential of the Janus nanoparticles and magnetically-enhanced photothermia *in vitro*

We next investigated an alternative asset from the magnetic component: the possibility for the nanoparticles to be remotely guided by a magnet. To test how such a magnetic guidance can enhance the capture of Janus nanoparticles by cancer cells, we focused on Fe(20)@Au, because of their larger magnetic diameter of 20 nm, associated with a higher photothermal potential. With this strategy, the cytotoxic heating response of nanoparticles may be amplified inside cells for a more efficient photothermal therapeutic effect. Cells were then incubated with Fe(20)@Au for 3 hours, at the extracellular concentrations of [Fe] = 25, 50 and 100 µM. A permanent magnet (B = 0.2 T, grad B = 50 T/m) was placed (MAGNET condition) or not (NO MAGNET) below the culture dishes during all incubation. The permanent magnet was removed after the incubation protocol. The cellular uptake of nanoparticles was measured at the single cell level by magnetophoresis, which allows quantifying the iron mass per cell, m_{Fe}, as shown in **Figure**

4A. The nanoparticles internalization was clearly boosted by the use of the external magnet (MAGNET), yielding values per cell at 1.3-4.5 pg_{Fe} versus 0.2-0.5 pg_{Fe} for the NO MAGNET condition. For each condition, the cells (3 million) were detached after incubation, and suspended in 50 µL medium. Figure 4B shows the resulting cell pellets, which feature a dark color perfectly illustrating the enhanced uptake under the magnetic field. As a consequence, the photothermal response was also remarkably increased under application of the magnet. Figures 4C and 4D show the thermal images and temperature elevation curves after 5 min of 680 nm-laser irradiation at 0.5 W/cm². Magnetically-guided PTT was significantly more effective (Figure 4E), especially at the lowest extracellular dose of [Fe] = 25 µM: temperature elevation then increased from 12 °C (NO MAGNET) up to 28 °C (MAGNET). The corresponding concentrations for each condition are also indicated in Figure 4E: incubation at 25, 50, 100 µM with magnet resulted in cellular pellet concentration of [Fe] = 2.4, 3.2, 4.6 mM versus [Fe] = 0.15, 0.3, 0.6 mM without magnet. These pellet concentrations are in perfect agreement with temperature increments reported in Figures 2 and 3, for nanoparticles in aqueous dispersion or in cells, respectively. TEM images (Figure 4F) confirmed the enhanced internalization of the nanoparticles under magnet application, with more nanoparticles observed per cell, densely packed within endosomes.

The magnetic attraction potential of the Janus nanoparticles was finally also evidenced by the formation of chains of endosomes containing the nanoparticles within the cells (Figure 4G), upon application of a 0.2 T horizontal magnetic field created by two magnets facing each other around the cells dish. Iron specific Prussian blue staining of the cells was performed after 1 h of magnetic field application, revealing the numerous chaining of endosomes between them, along the magnetic field lines.

The Janus design allows providing magneto-plasmonic nanomaterials with such a highly efficient branched-shell morphology on one side (based on gold nanostars as the most efficient

gold-based photothermal agents), and all magnetic-based functions for magnetic hyperthermia and guiding on the other side.

2.5. Magnetically-guided photothermal treatment with Janus nanoparticles *in vivo*

The final step was to evaluate *in vivo* the combined action of Janus nanoparticles for magnetic guidance toward the tumor site and subsequent photothermal treatment. 200 µL of Fe(20)@Au suspension ([Fe] = 3.5 mM and [Au] = 8 mM**)** were administered by intravenous tail injection in CT-26 tumor-bearing mice. A small permanent magnet generating a 0.2 T magnetic field was positioned on the mouse tumor for the MAGNET group. The objective was to generate a higher concentration of nanoparticles around the tumor tissue, where the magnet was placed. 24 hours after magnet application, tumors were irradiated with 680 nm laser (0.8 W cm^{-2}, 1 cm spot diameter) for 15 min. The NO MAGNET group corresponded to intravenously-injected and irradiated tumors without the magnet application. Non-injected but irradiated tumors were considered as treated controls (LASER ONLY) and non-injected and non-treated as normal controls (CONTROL). The average tumor local temperatures after 15 min of laser irradiation are displayed in **Figure 5**A. The increase of temperature at the tumor region in the MAGNET group reached $\Delta T = 20 \pm 2$ °C, which corresponds to a final temperature around 48 ± 4 °C. This temperature elevation is almost 2-fold that for the NO MAGNET group ($\Delta T = 13 \pm 2$ °C), heated at temperatures of about 41 ± 2 °C. The increase of temperature only considering the effect of laser heating (LASER ONLY) at the tumor region is $\Delta T = 10 \pm 1$ °C.

The increased temperature or the MAGNET group indicates an enhanced accumulation of nanoparticles around the tumor tissue mediated by the magnetic field application. The tumor-bearing mice were then monitored for tumor growth status every day after the treatment (Figure 5B). Compared to the control, magnetic-guided and photothermally treated mice (MAGNET) exhibited tumor growth inhibition, even at day 8 after treatment. Comparatively, even if the photothermal-treated group without magnetic guiding of nanoparticles (NO MAGNET) did

reduce tumor growth, it was not fully inhibited, exhibiting a still significant progression of the malignant tissue.

Histological staining of tumors (Prussian Blue and hematoxylin/eosin (H&S)) was performed at the end of tumor progression monitoring (8 days post-treatment), as shown in Figure 5C. Prussian blue staining revealed iron-positive areas in mice, injected with nanoparticles under magnetic-guided targeting (MAGNET) while for those without targeting (NO MAGNET), nanoparticles were hardly detected. The H&S staining revealed no clear damage effect for the NO MAGNET treated condition compared with the control, where dense and connected tissue was observed. However, tissue damage was clearly identified in the MAGNET treated tumor sections, with a loss of cell cohesion and necrotic areas.

In order to quantify the effective nanoparticle accumulation in tumor tissues, the magnetic response of the tumors were investigated 24 hours after injection (equivalent to treatment day). Typical magnetization curves at room temperature of excised tumors without and with magnet application are displayed in Figures 5D and 5E, respectively. Higher magnetization (in μemu) is clearly observed for mice under the MAGNET condition. Magnetization can be converted into mass of iron (or equivalently mass of nanoparticles, Fe_3O_4+Au), leading to values of 14 ± 2 $\mu g_{Fe}/g_{tum}$ versus 9 ± 3 $\mu g_{Fe}/g_{tum}$ for MAGNET and NO MAGNET conditions respectively. In terms of total mass of nanoparticles (μg_{Fe}, iron) reaching the tumor (after renormalizing by the each tumor total mass), the MAGNET and NO MAGNET conditions correspond to 1.3 ± 0.3 μg_{Fe} and 0.6 ± 0.2 μg_{Fe}, respectively. The averaged total mass (in μg_{Fe}) of accumulated nanoparticles in tumors is shown in Figure 5F for both MAGNET and NO MAGNET conditions, clearly evidencing the potential of the magnetic guiding strategy to accumulate nanoparticles at tumor site. The NO MAGNET condition represents the passive accumulation of nanoparticles in tumors due to the enhanced permeability and retention (EPR) effect. For subcutaneous tumors with low vascularization, the EPR effect generally achieves accumulation of about 1 % of nanoparticles, related to the injected dose.[45] Here, considering that 60 μg_{Fe}

was injected intravenously, the EPR outcome for the NO MAGNET group is 1.5 % of the injected dose. Remarkably, for the MAGNET condition, this value is increased to 3.4 %, which is a very significant value for a targeting strategy.[14a, 46]

3. Conclusions

We have explored the use of Janus gold-iron oxide nanoparticles as heat generators when subjected to stand-alone or combined MHT and PTT protocols, according to different parameters of application such as nanoparticle design (both magnetic and plasmonic), nanoparticle concentration, and exposure settings. In general terms, MHT is found to be effective at high nanoparticle dose, while PTT is much more suitable at low doses. MHT efficiency is severely affected by cellular uptake, with only minor magneto-active heating observed in the cellular environment. However, when combined with PTT, MHT displays again a synergistic cytotoxic effect, with the dual modality (PTT + MHT) killing almost all cancer cells (< 5 % of cell viability).

Regarding a second virtue of the magnetic component, we have explored the use of Janus nanoparticles for targeting, under application of an external field gradient. Cellular internalization of the nanoparticles was largely enhanced by the use of a magnet during incubation, thus revealing a more effective photothermal therapy of cancer cells *in vitro*. Magnetic-guided photothermal therapy was also tested *in vivo*, using a one shot exposure at moderate laser power (0.8 W/cm^2, 680 nm). Under the application of a magnet, increased nanoparticle concentration was achieved at the tumor site after systemic intravenous injection, which in turn elicited an improved therapeutic action, which led to total tumor inhibition growth. Janus magnetic-plasmonic nanoparticles are therefore positioning themselves as effective therapeutic tools to be delivered by blood for cancer nano-therapy.

4. Experimental section

Chemicals

All chemicals were used as received, without further purification: hydrogen tetrachloroaurate(III) trihydrate (99.99%, Alfa Aesar), oleylamine (80-90%, Acros Organics), 1-octadecene (90%, Aldrich), oleic acid (90%, Aldrich), iron(0) pentacarbonyl (99.99%, Aldrich), 1,2-hexadecanediol (90%, Aldrich), methoxypolyethylene glycol acetic acid (PEG, 80%, Mn = 5000 g/mol), polyvinylpyrrolidone (PVP, Mn=10000 g/mol, Aldrich), additional solvents were reagent grade from Aldrich.

Synthesis of Janus magnetic nanostars

The Janus magnetic nanostars were synthesized as previously reported.[29] Starting with the synthesis of asymmetric gold-iron oxide heterodimers and a further nanostar growing step.

Asymmetric heterodimers with 16 and 20 nm iron oxide lobe

The synthesis of heterodimers with 16 nm iron oxide lobe was carried out as previously reported.[20a, 29] A solution in 1-octadecane (40 mL) was prepared containing oleic acid (6 mmol, 1.90 mL), oleylamine (6 mmol, 1.97 mL) and 1,2-hexadecanediol (10 mmol, 2.58 g) and stirred for 20 min at 120 ºC under N_2. $Fe(CO)_5$ (0.3 mL) was then injected and after 3 min a solution containing $HAuCl_4 \cdot 3H_2O$ (0.1 mmol) dissolved in a mixture of oleylamine (0.5 mL) and 1-octadecane (5 mL) was injected and heated up to 300 °C at approximately 1 °C/min. The solution was left to react for 45 min under magnetic stirring. After cooling down, the dispersion was exposed to air for 30 min to cause Fe oxidation.[47]

The synthesis of the 20 nm sample was similar but adding 2 mL of $Fe(CO)_5$ at 160 °C. In this case the sample was mechanically stirred (instead of magnetically) and was heated up to 310 °C. To purify the nanoparticles, 50 mL of isopropanol was added and the solution centrifuged at 4500 g for 30 min. The nanoparticles were cleaned two more times after redispersion with hexane and aggregation with isopropanol. Finally, oleylamine (100 μL) was added to store the nanoparticles for long periods of time in a hexane-chloroform solution.

Janus magnetic nanostars

The heterodimers were cleaned three times in ethanol and redispersed in a small quantity of chloroform to remove as much as oleylamine as possible. Finally, they were redispersed in chloroform at a concentration of 2 mg/mL. A small quantity of carboxyl-terminated PEG was added to the solution (to have approximately 2 mg/mL of polymer) and left for 1h stirring. This step was performed to obtain a good dispersion when the seeds were added to the DMF gold precursor solution.

A solution of $HAuCl_4 \cdot 3H_2O$ (2.184 mL, 50 mM) was added to a solution of polyvinylpyrrolidone (PVP) (40 g, MW = 10 Kg/mol) in DMF (400 mL). The freshly prepared solution was left stirring to allow gold salt prereduction from Au^{3+} to Au^{+} as described elsewhere[30] (this time was highly dependent on the PVP batch and needed to be adjusted by UV-vis spectroscopy, in this case it was 5 min). The dumbbell nanoparticle colloid (4.65 mL for Fe(20)@Au and 4.3 mL for Fe(16)@Au) was then quickly added and the reaction was left reacting for 1 h, showing a fast color change into blue. The nanoparticles were purified in 4 centrifugation cycles, redispersed 2 times in ethanol and 2 times in water and at a relative centrifugation force of 2500-4000 g, depending on the nanoparticle size. The nanoparticles were finally redispersed in 40 mL of ultrapure water.

Elemental analysis

Elemental analysis was performed by inductively coupled plasma mass spectrometry (ICP-MS) with a helium collision cell. An internal standard was introduced by adding 100 μL of Yttrium at 500 ppb. The measured selected isotopes to perform the quantification were ^{57}Fe and ^{197}Au. The aqueous solution for ICP was prepared by adding 200 μL of aqua regia to a 50 μL solution of nanoparticles and left for 30 min. The sample was then diluted to have a final volume of 3 mL.

Transmission electron microscopy (TEM)

TEM images were acquired in a JEOL JEM-1400PLUS instrument operating at 120 kV, after nanoparticles were deposited on a carbon coated TEM grid. The nanoparticles morphological

features were analyzed with the Image J software package. Energy-dispersive X-ray spectroscopy (EDX) mapping were obtained in a JEOL JEM-2100F UHR (80 kV–200 kV), equipped with STEM and OXFORD INCA EDXS systems.

Scanning electron microscopy (SEM)

SEM images were measured in a Hitachi S4800 equipped with a FEG gun. Nanoparticles were deposited on a Si wafer, dried and inserted in the instrument without further coating. The measurement was performed at energies between 5 and 10 KeV.

X-ray diffraction (XRD)

X-ray powder diffraction patterns were collected by using a Philips X'pert PRO automatic diffractometer operating at 40 kV and 40 mA, in theta-theta configuration, secondary monochromator with Cu-Kα radiation (λ = 1.5418 Å) and a PIXcel solid state detector (active length in 2θ 3.347º). Data were collected from 5 to 90° 2θ, step size 0.026º and time per step of 300s at RT. 1º fixed soller slit and divergence slit giving a constant volume of sample illumination were used.

UV-Vis-NIR spectroscopy

The absorbance of nanoparticle solutions was recorded using a Cary 8453 UV-Vis diode array spectrophotometer (Agilent) over the 300−1100 nm range of wavelengths. The absorption and scattering contributions of the total extinction were quantified using a home-made diffuse reflectance setup using a $BaSO_4$-coated integrating sphere (UPB-150-ART, Gigahertz-Optik), equipped with a white-light halogen source (HL-2000-FHSA, Ocean Optics), a light trap (UPB-150-ART-Z04), and a spectrometer (MAYA Pro, Ocean Optics) as detector.[37] For the measurements, a quartz glass cuvette with four clear sides was positioned at the center of the integrating sphere and a fixed set of measurements was performed as described by Höller *et al.*[36a]: sample measured without light trap (scattered and transmitted light); sample measured with light trap (scattered light); and water measured without light trap (as background).

Electromagnetic simulations

Numerical simulations were performed using the commercial software FDTD Solutions (v.8.23.2152) from Lumerical Solutions, Inc. The dielectric functions were fitted to tabulated experimental data by Johnson and Christy for Au and by Querry for Fe_3O_4 (RMS errors <0.9, **Figure S2**).[48] The background index was set to 1.33 to mimic water. Total-field scattered-field (TFSF) plane-wave sources, ranging from 400 to 1000 nm, were used to separate the computation region into two distinct regions – one containing the total field (*i.e.*, the sum of the incident field and the scattered field), and another that contains only the scattered field. Mesh values were set to 1 nm for the empty space and 0.5 nm for the particle space. All simulations reached a convergence of 10^{-7} before reaching 300 fs simulation time.

Magneto- and photothermal effect measurements in aqueous suspensions

Nanoparticles in aqueous dispersion (at the concentrations [Fe] = 0.05 to 24 mM for Fe(20)@Au and [Fe] = 12 to 48 mM for Fe(16)@Au) contained in a 0.5 mL-tube (150 uL) were subjected to an alternating magnetic field (MHT) at 470 kHz of frequency and 18 mT of field, irradiated with a 680 nm laser (PTT) at the power of 0.5 W cm^{-2} (spot size of 1 cm^2), or both effects at the same time (DUAL). The temperature values were recorded with a real-time infrared thermal imaging camera (FLIR SC7000, FLIR Systems, USA). The heating capabilities were quantified using the SAR parameter (Specific Absorption Rate) determined experimentally using the formula:

$$SAR = \frac{C_V}{m_{Fe3O4 + Au}} . \frac{dT}{dt}$$

where (dT/dt) is the temperature rise slope at early times (first 30 s) to simulate adiabatic conditions, C_v the volumetric specific heat capacity of the sample (C_{water} =4185 J L^{-1} K^{-1}) and $m_{Fe3O4 + Au}$ is the mass of nanoparticles.

The photothermal SAR can also be expressed as follows:

$$SAR = \frac{1}{m_{Fe3O4 + Au}} . [I_0 . S . (1\text{-}10^{-A}) . \eta]$$

where I_0 is incident laser power in W, S is the illuminated area in cm^2, A is the optical absorbance (following the Beer-Lambert law) at the selected wavelength (680 nm) and η is the photothermal conversion coefficient.

Cell culture, incubation of nanoparticles and uptake quantification

Murine colorectal carcinoma cell lines (CT-26) were purchased from ATCC®. CT-26 cells were cultured with Dulbecco's modified Eagle medium (DMEM) supplemented with 5 % FBS and 1% penicillin at 37 °C in a 5 % CO_2 environment.

Cells were incubated with Fe(16)@Au or Fe(20)@Au nanoparticles at the extracellular concentration of [Fe] = 20-100 µM, for 24 h (for the evaluation of nanoparticle internalization profile) and for 3 h (for the evaluation of magnetic targeting uptake effect in the presence of a permanent magnet (MAGNET condition) or not (NO MAGNET)) in DMEM medium supplemented with 5 % FBS. At the end of the incubation time, the medium was then removed, the labeled cells were washed with culture medium and detached. Inductively coupled plasma atomic emission spectroscopy (ICP-AES) and magnetophoresis were used to quantify the amount of iron and gold either per single cell (in pg/cell). They were then resuspended at a concentration of about 5 million cells in 50 µL of culture medium adjusted to match [Fe] in the range of 1.5-6 mM. Magnetophoresis measurements consist of tracking labeled cells subjected to a magnetophoretic flow due to the presence of a permanent magnet (B = 0.14 T, grad B = 17 T/m). The magnetic moment of each cell (M_{cell}) is obtained after balancing the magnetic force ($M_{cell} \cdot gradB$) and drag force ($6\pi\eta \cdot r_{cell} \cdot v_{cell}$, where η is the viscosity of the suspension medium, r_{cell} and v_{cell} are the radius and velocity of the cell, respectively) by calculating the motion (velocity and size) of 50 cells with a camera coupled to an optical microscope. The magnetic m_{Fe} per cell can be thus obtained considering the calculated M_{cell} (emu) and the magnetization curves (emu/g_{Fe}) from VSM measurements (providing relative magnetization at 140 mT and the saturation magnetization).

***In vitro* magneto- and photothermal study**

A magneto- and photo-induced heating experiment *in vitro* was designed to evaluate the thermal capabilities of Fe(20)@Au and Fe(16)@Au samples. Labelled cell pellets as described above were subjected to the same experimental protocols as the aqueous solution samples: an alternating magnetic field (MHT, 470 kHz and 18 mT), 680 nm-laser irradiation (PTT) at the power of 0.5 W/cm^2, and both effects at the same time (DUAL).

Viability assay

Cell viability was assessed by Alamar blue assay, according to the supplier's protocol (Life Technologies). After applying the individual and combined treatments, the cells in suspension were computed and seeded in 24-well plates with complete culture medium. An Alamar Blue solution (10% in DMEM without red phenol) was added, incubated for 2 h, and then transferred to a 96-well plate. The fluorescence was analyzed by a microplate reader (excitation 570 nm, emission 585 nm, SpectraMax M5, Molecular Devices). Viability was normalized with unlabeled control cells. All reported experimental results were done in triplicate. A thermostated device was used to ensure physiological temperature conditions (37 °C).

Magnetic properties

The magnetic characterization of samples in aqueous suspension and internalized in cells was carried out using a Vibrating Sample Magnetometer (VSM, Quantum Design, Inc.) at the Paris Sorbonne University, France. Magnetization curves were measured at 300 K as a function of the external field (till saturation, 3T). For cells, a sample corresponding to about 4 x 10^5 cells dispersed in 20 µL was measured (each cell containing 3 pg of Fe in average). The magnetization curves are shown in emu/g_{Fe}.

X-ray absorption measurements (XAS)

XAS measurements in the XANES *(*X-ray absorption near edge structure) and in the EXAFS (Extended X-Ray Absorption Fine Structure) regimes were performed at the CRG beamline (BM25-SpLine) of the European Synchrotron Radiation Facilities (ESRF) in Grenoble (France). The spectra were acquired at the Au L-edge (11919 eV) at room temperature in the transmission

mode using ionization chambers as detectors. An Au foil was measured as a reference and during the measurements to correct energy drifts by using a third ionization chamber. Data reduction and analysis of the XAS data were carried out using the Demeter package software identifying the absorption edge (E_0).[4]

***In vivo* magnetically-guided photothermal experiment**

All procedures involving animals were performed in accordance with the European standards of animal care and well-being use of Animalerie Buffon (Institute Jacques Monod, Paris). Six-week-old female BALB/cJRj mice (weighing 30 g, provided by Janvier, France) (a total of 17) were used in this study. All animal experiments were approved by Buffon ethics committee (Project Ref. No. CEB-07-2016). In order to induce solid tumors, CT-26 cells (1×10^6) in 0.1 mL of PBS were injected subcutaneously in the right and left flanks of mice. Tumors were allowed to grow for about 3 weeks until the volume was approximately 125 mm^3. The tumor volume was calculated as V = length × width^2/2 using a caliper. 200 µL of Fe(20)@Au saline dispersion ([Fe] = 3.5 mM and [Au] = 8 mM**,** corresponding to 1.3 mg/kg of Fe and 10.5 mg/kg of Au) was intravenously (i. v.) injected into tail of tumor-bearing mice the previous day. In some of them an external magnet was placed closed to the tumor area (cylindrical magnet, 10 × 5 mm, grad B = 17 T/m). Twenty-nine tumors in 17 animals were divided into several groups: MAGNET (i. v. injected, PTT treated, external magnet field, n = 8), NO MAGNET (i. v. injected, PTT treated, no external magnet field, n = 8), LASER ONLY (non-injected, PTT treated, n = 7), and CONTROL (non-injected, non-treated, n = 6). The PTT treatment consisted on the illumination of CT-26 tumor-bearing mice with the 680 nm laser (at 0.8 W/cm^2) for 15 min. During the treatment, mice were anesthetized with isoflurane. An infrared thermal camera (FLIR SC7000, FLIR Systems, USA) was used to monitor the temperature over the tumor region. The animals were sacrificed before tumors reached 1 cm^3. Small excisions of harvested tumors were also analyzed in the VSM to obtain the magnetization versus magnetic field curves (in µemu) at 300 K. The saturation magnetization obtained in cells (around 70 emu/g_{Fe} in cells,

Figure S6) was applied to estimate the concentration of iron (and then, of nanoparticles) in the tumors with or without an external magnetic field (MAGNET or NO MAGNET condition).

Histological and microscopy analysis of tumors

Mice were sacrificed 8 days after each treatment and the tumors were harvested. The tumors were fixed in buffered formalin-saline (10%) overnight. Then they were embedded in paraffin, cut in 5 μm thick slices that were stained with hematoxylin/eosin (H&S) and Prussian Blue (performed at Cochin HistIM Facility) and analyzed by optical microscopy.

Unlabeled/labeled cells or 1 mm^3 tumor tissue pieces were fixed for 2 h with 2% glutaraldehyde in 0.1 M cacodylate buffer (7.4 pH) at 4 °C. Then they were post-fixed with 1% osmium tetroxide and 1.5% potassium cyanoferrate in cacodylate buffer. They were subsequently dehydrated in ethanol, and embedded in Epon resin. Thin slices of 70 nm were collected onto copper grids and observed with a Hitachi HT 7700 TEM operated at 80 kV (MIMA2 platform, INRA, Jouy-en-Josas, France).

Conflicts of interest

There are no conflicts to declare.

Supporting Information

Supporting Information is available from the Wiley Online Library or from the author.

Acknowledgments

This work was supported by the European Union (Marie Curie Intra-European Project FP7-PEOPLE-2013-740 IEF-62647). AE acknowledges the support by Comunidad de Madrid (Talento project 2018-T1/IND-1005 and NANOMAGCOST project 2018/NMT-4321), MINECO project SEV-2016-0686 and AECC project Ideas Semilla 2019. AMN acknowledges the support by Comunidad de Madrid (Talento project 2018-T1/IND-10360). CK acknowledges financial support from the European Commission under the Marie Skłodowska-Curie program (H2020-MSCA-799393, NANOBIOME). LML-M acknowledges support from MINECO project MAT2017-86659-R and Maria de Maeztu Units of Excellence Program from the

Spanish State Research Agency (Grant No. MDM-2017-0720). We are grateful to Christine Péchoux for TEM preparation (INRA in Jouy-en-Josas, Paris, France), Ludovic Maingault and Isabelle Le Parco for their help in animal studies (Jacques Monod Institute, Paris, France). The authors thank Andreas Seifert (CIC nanoGUNE) for providing access to the diffuse reflectance setup and scientific discussion. We acknowledge the ESRF for beamtime and the CRG beamline BM25-SpLine personnel for technical support. The authors thank for technical and human support provided by SGIker (UPV/EHU/ ERDF, EU)

References

[1] a) V. Wagner, A. Dullaart, A.-K. Bock, A. Zweck, *Nature biotechnology* **2006**, *24*, 1211; b) G. T. Tietjen, W. M. Saltzman, *Sci Transl Med* **2015**, *7*, 314fs47.

[2] a) J. Shi, P. W. Kantoff, R. Wooster, O. C. Farokhzad, *Nature Reviews Cancer* **2017**, *17*, 20; b) A. Nicolas-Boluda, A. K. Silva, S. Fournel, F. Gazeau, *Biomaterials* **2017**.

[3] a) R. Hergt, S. Dutz, R. Müller, M. Zeisberger, *Journal of Physics: Condensed Matter* **2006**, *18*, S2919; b) D. Jaque, L. M. Maestro, B. Del Rosal, P. Haro-Gonzalez, A. Benayas, J. Plaza, E. M. Rodríguez, J. G. Solé, *Nanoscale* **2014**, *6*, 9494.

[4] R. E. Rosensweig, *Journal of magnetism and magnetic materials* **2002**, *252*, 370.

[5] a) R. Weissleder, Nature Publishing Group, 2001; b) A. M. Smith, M. C. Mancini, S. Nie, *Nature Nanotechnology* **2009**, *4*, 710.

[6] P. K. Jain, X. Huang, I. H. El-Sayed, M. A. El-Sayed, *Acc. Chem. Res.* **2008**, *41*, 1578.

[7] A. Espinosa, J. Kolosnjaj‐Tabi, A. Abou‐Hassan, A. Plan Sangnier, A. Curcio, A. K. Silva, R. Di Corato, S. Neveu, T. Pellegrino, L. M. Liz‐Marzán, *Adv. Funct. Mater.* **2018**, *28*, 1803660.

[8] a) J. W. Bulte, D. L. Kraitchman, *NMR in Biomedicine* **2004**, *17*, 484; b) A. K. Andriola Silva, R. Di Corato, F. Gazeau, T. Pellegrino, C. Wilhelm, *Nanomedicine* **2012**, *7*, 1713; c) V. V. Mody, A. Cox, S. Shah, A. Singh, W. Bevins, H. Parihar, *Applied Nanoscience* **2014**, *4*, 385.

[9] a) K.-S. Lee, M. A. El-Sayed, *The Journal of Physical Chemistry B* **2006**, *110*, 19220; b) X. Wu, F. Yang, T. Ming, R. Xiong, P. Wang, J. Chen, *Applied Physics Letters* **2011**, *98*, 213704; c) E. M. Larsson, J. Alegret, M. Käll, D. S. Sutherland, *Nano Letters* **2007**, *7*, 1256.

[10] Y. Vasquez, M. Kolle, L. Mishchenko, B. D. Hatton, J. Aizenberg, *ACS Photonics* **2013**, *1*, 53.

[11] a) C. Wang, Y. Yao, Q. Song, *J. Mater. Chem. C* **2015**, *3*, 5910; b) G. Wang, W. Gao, X. Zhang, X. Mei, *Scientific Reports* **2016**, *6*, 28258.

[12] a) C. H. Wu, J. Cook, S. Emelianov, K. Sokolov, *Adv. Funct. Mater.* **2014**, *24*, 6862; b) L. H. Silva, J. R. Silva, G. A. Ferreira, R. C. Silva, E. C. Lima, R. B. Azevedo, D. M. Oliveira, *J. Nanobiotechnol.* **2016**, *14*, 59.

[13] a) J. Huang, M. Guo, H. Ke, C. Zong, B. Ren, G. Liu, H. Shen, Y. Ma, X. Wang, H. Zhang, *Advanced Materials* **2015**, *27*, 5049; b) M. Khafaji, M. Vossoughi, M. R. Hormozi-Nezhad, R. Dinarvand, F. Börrnert, A. Irajizad, *Scientific Reports* **2016**, *6*, 27847; c) X. Chen, G. Li, Q. Han, X. Li, L. Li, T. Wang, C. Wang, *Chemistry–A European Journal* **2017**, *23*, 17204; d) W. Feng, X. Zhou, W. Nie, L. Chen, K. Qiu, Y.

Zhang, C. He, *ACS Appl. Mater. Inter.* **2015**, *7*, 4354; e) C. Hoskins, Y. Min, M. Gueorguieva, C. McDougall, A. Volovick, P. Prentice, Z. Wang, A. Melzer, A. Cuschieri, L. Wang, *J. Nanobiotechnol.* **2012**, *10*, 27; f) D. K. Kirui, I. Khalidov, Y. Wang, C. A. Batt, *Nanomedicine* **2013**, *9*, 702; g) G. A. Sotiriou, F. Starsich, A. Dasargyri, M. C. Wurnig, F. Krumeich, A. Boss, J. C. Leroux, S. E. Pratsinis, *Adv. Funct. Mater.* **2014**, *24*, 2818; h) J. Kim, S. Park, J. E. Lee, S. M. Jin, J. H. Lee, I. S. Lee, I. Yang, J. S. Kim, S. K. Kim, M. H. Cho, *Angewandte Chemie* **2006**, *118*, 7918; i) I. Urries, C. Muñoz, L. Gomez, C. Marquina, V. Sebastian, M. Arruebo, J. Santamaria, *Nanoscale* **2014**, *6*, 9230; j) C. Li, T. Chen, I. Ocsoy, G. Zhu, E. Yasun, M. You, C. Wu, J. Zheng, E. Song, C. Z. Huang, *Adv. Funct. Mater.* **2014**, *24*, 1772.

[14] a) H. J. Kim, S.-M. Lee, K.-H. Park, C. H. Mun, Y.-B. Park, K.-H. Yoo, *Biomaterials* **2015**, *61*, 95; b) N. S. Elbialy, M. M. Fathy, W. M. Khalil, *Int. J. Pharm.* **2015**, *490*, 190; c) Z. Fan, M. Shelton, A. K. Singh, D. Senapati, S. A. Khan, P. C. Ray, *ACS Nano* **2012**, *6*, 1065.

[15] a) A. Espinosa, M. Bugnet, G. Radtke, S. Neveu, G. A. Botton, C. Wilhelm, A. Abou-Hassan, *Nanoscale* **2015**, *7*, 18872; b) R. Das, N. Rinaldi-Montes, J. Alonso, Z. Amghouz, E. Garaio, J. García, P. Gorria, J. Blanco, M. Phan, H. Srikanth, *ACS Appl. Mater. Inter.* **2016**, *8*, 25162; c) M. Abdulla-Al-Mamun, Y. Kusumoto, T. Zannat, Y. Horie, H. Manaka, *RSC Adv.* **2013**, *3*, 7816.

[16] a) S. Shen, F. Kong, X. Guo, L. Wu, H. Shen, M. Xie, X. Wang, Y. Jin, Y. Ge, *Nanoscale* **2013**, *5*, 8056; b) S. Shen, S. Wang, R. Zheng, X. Zhu, X. Jiang, D. Fu, W. Yang, *Biomaterials* **2015**, *39*, 67; c) M. Chu, Y. Shao, J. Peng, X. Dai, H. Li, Q. Wu, D. Shi, *Biomaterials* **2013**, *34*, 4078.

[17] A. Espinosa, R. Di Corato, J. Kolosnjaj-Tabi, P. Flaud, T. Pellegrino, C. Wilhelm, *ACS Nano* **2016**, *10*, 2436.

[18] a) L. Huang, L. Ao, D. Hu, W. Wang, Z. Sheng, W. Su, *Chemistry of Materials* **2016**, *28*, 5896; b) S. Bhana, G. Lin, L. Wang, H. Starring, S. R. Mishra, G. Liu, X. Huang, *ACS Appl. Mater. Inter.* **2015**, *7*, 11637; c) H.-W. Yang, H.-L. Liu, M.-L. Li, I.-W. Hsi, C.-T. Fan, C.-Y. Huang, Y.-J. Lu, M.-Y. Hua, H.-Y. Chou, J.-W. Liaw, *Biomaterials* **2013**, *34*, 5651.

[19] a) K.-L. Chen, Y.-W. Yeh, J.-M. Chen, Y.-J. Hong, T.-L. Huang, Z.-Y. Deng, C.-H. Wu, S.-H. Liao, L.-M. Wang, *Scientific Reports* **2016**, *6*, 35477; b) E. D. Smolensky, M. C. Neary, Y. Zhou, T. S. Berquo, V. C. Pierre, *Chemical Communications* **2011**, *47*, 2149; c) T. A. Larson, J. Bankson, J. Aaron, K. Sokolov, *Nanotechnology* **2007**, *18*, 325101; d) X. Ji, R. Shao, A. M. Elliott, R. J. Stafford, E. Esparza-Coss, J. A. Bankson, G. Liang, Z.-P. Luo, K. Park, J. T. Markert, *J. Phys. Chem. C* **2007**, *111*, 6245.

[20] a) H. Yu, M. Chen, P. M. Rice, S. X. Wang, R. White, S. Sun, *Nano Letters* **2005**, *5*, 379; b) C. Xu, J. Xie, D. Ho, C. Wang, N. Kohler, E. G. Walsh, J. R. Morgan, Y. E. Chin, S. Sun, *Angewandte Chemie International Edition* **2008**, *47*, 173.

[21] a) F. Bertorelle, M. Pinto, R. Zappon, R. Pilot, L. Litti, S. Fiameni, G. Conti, M. Gobbo, G. Toffoli, M. Colombatti, *Nanoscale* **2018**, *10*, 976; b) J. A. Hachtel, S. Yu, A. R. Lupini, S. T. Pantelides, M. Gich, A. Laromaine, A. Roig, *Faraday Discussions* **2016**, *191*, 215.

[22] L. L. Ma, M. D. Feldman, J. M. Tam, A. S. Paranjape, K. K. Cheruku, T. A. Larson, J. O. Tam, D. R. Ingram, V. Paramita, J. W. Villard, *ACS Nano* **2009**, *3*, 2686.

[23] a) J. Reguera, H. Kim, F. Stellacci, *CHIMIA Int. J. Chem.* **2013**, *67*, 811; b) J. Zhang, B. A. Grzybowski, S. Granick, *Langmuir* **2017**, *33*, 6964; c) J. Hu, S. Zhou, Y. Sun, X. Fang, L. Wu, *Chem. Soc. Rev.* **2012**, *41*, 4356; d) A. Walther, A. H. Müller, *Chemical Reviews* **2013**, *113*, 5194.

[24] a) D. J. Cole-Hamilton, *Science* **2010**, *327*, 41; b) X. Ma, K. Hahn, S. Sanchez, *Journal of the American Chemical Society* **2015**, *137*, 4976; c) S. T. Kochuveedu, Y. H. Jang, D. H. Kim, *Chemical Society Reviews* **2013**, *42*, 8467; d) Q. Chen, J. K. Whitmer, S. Jiang, S. C. Bae, E. Luijten, S. Granick, *Science* **2011**, *331*, 199.
[25] a) K. Lee, L. Zhang, Y. Yi, X. Wang, Y. Yu, *ACS Nano* **2018**, *12*, 3646; b) K. Lee, Y. Yu, *Langmuir* **2018**, *34*, 12387; c) Q.-s. Xia, H.-m. Ding, Y.-q. Ma, *Nanoscale* **2017**, *9*, 8982.
[26] P. Yánez-Sedeño, S. Campuzano, J. Pingarrón, *Applied Materials Today* **2017**, *9*, 276.
[27] G. Rucinskaite, S. A. Thompson, S. Paterson, R. De La Rica, *Nanoscale* **2017**, *9*, 5404.
[28] J. Reguera, D. J. de Aberasturi, N. Winckelmans, J. Langer, S. Bals, L. M. Liz-Marzán, *Faraday Discussions* **2016**, *191*, 47.
[29] J. Reguera, D. Jiménez De Aberasturi, M. Henriksen-Lacey, J. Langer, A. Espinosa, B. Szczupak, C. Wilhelm, L. M. Liz-Marzán, *Nanoscale* **2017**, *9*, 9467.
[30] S. Barbosa, A. Agrawal, L. Rodríguez-Lorenzo, I. Pastoriza-Santos, R. A. Alvarez-Puebla, A. Kornowski, H. Weller, L. M. Liz-Marzán, *Langmuir* **2010**, *26*, 14943.
[31] A. Espinosa, A. K. Silva, A. Sánchez‐Iglesias, M. Grzelczak, C. Péchoux, K. Desboeufs, L. M. Liz‐Marzán, C. Wilhelm, *Advanced Healthcare Materials* **2016**, *5*, 1040.
[32] a) M. Grzelczak, J. Pérez-Juste, P. Mulvaney, L. M. Liz-Marzán, *Chemical Society Reviews* **2008**, *37*, 1783; b) N. Almora-Barrios, G. Novell-Leruth, P. Whiting, L. M. Liz-Marzan, N. Lopez, *Nano letters* **2014**, *14*, 871.
[33] a) E. Ye, K. Y. Win, H. R. Tan, M. Lin, C. P. Teng, A. Mlayah, M.-Y. Han, *Journal of the American Chemical Society* **2011**, *133*, 8506; b) L. Zhang, Y. Chen, Z. Li, L. Li, P. Saint‐Cricq, C. Li, J. Lin, C. Wang, Z. Su, J. I. Zink, *Angewandte Chemie International Edition* **2016**, *55*, 2118.
[34] P. S. Kumar, I. Pastoriza-Santos, B. Rodriguez-Gonzalez, F. J. G. De Abajo, L. M. Liz-Marzán, *Nanotechnology* **2007**, *19*, 015606.
[35] a) B. Chertok, B. A. Moffat, A. E. David, F. Yu, C. Bergemann, B. D. Ross, V. C. Yang, *Biomaterials* **2008**, *29*, 487; b) C. Sun, C. Fang, Z. Stephen, O. Veiseh, S. Hansen, D. Lee, R. G. Ellenbogen, J. Olson, M. Zhang, **2008**; c) M.-S. Martina, J.-P. Fortin, L. Fournier, C. Ménager, F. Gazeau, O. Clément, S. Lesieur, *Molecular imaging* **2007**, *6*, 7290.2007. 00004.
[36] a) R. P. Höller, M. Dulle, S. Thomä, M. Mayer, A. M. Steiner, S. Förster, A. Fery, C. Kuttner, M. Chanana, *ACS Nano* **2016**, *10*, 5740; b) C. Kuttner, R. P. Höller, M. Quintanilla, M. J. Schnepf, M. Dulle, A. Fery, L. M. Liz-Marzán, *Nanoscale* **2019**, *11*, 17655.
[37] M. Quintanilla, C. Kuttner, J. D. Smith, A. Seifert, S. E. Skrabalak, L. M. Liz-Marzán, *Nanoscale* **2019**, *11*, 19561.
[38] D. Chevrier, A. Chatt, T. Sham, P. Zhang, presented at Journal of Physics: Conference Series **2013**.
[39] a) J.-P. Fortin, C. Wilhelm, J. Servais, C. Ménager, J.-C. Bacri, F. Gazeau, *J. Am. Chem. Soc* **2007**, *129*, 2628; b) M. Gonzales-Weimuller, M. Zeisberger, K. M. Krishnan, *Journal of Magnetism and Magnetic Materials* **2009**, *321*, 1947.
[40] a) R. Di Corato, A. Espinosa, L. Lartigue, M. Tharaud, S. Chat, T. Pellegrino, C. Ménager, F. Gazeau, C. Wilhelm, *Biomaterials* **2014**, *35*, 6400; b) D. Cabrera, A. Coene, J. Leliaert, E. J. Artés-Ibáñez, L. Dupré, N. D. Telling, F. J. Teran, *ACS Nano* **2018**, *12*, 2741.
[41] A. L. Chen, Y. S. Hu, M. A. Jackson, A. Y. Lin, J. K. Young, R. J. Langsner, R. A. Drezek, *Nanoscale research letters* **2014**, *9*, 454.

[42] A. Plan Sangnier, S. Preveral, A. Curcio, A. K. A. Silva, C. T. Lefèvre, D. Pignol, Y. Lalatonne, C. Wilhelm, *J. Control. Release* **2018**, *279*, 271.
[43] a) X. Zhou, X. Lv, W. Zhao, T. Zhou, S. Zhang, Z. Shi, S. Ye, L. Ren, Z. Chen, *RSC Advances* **2018**, *8*, 18647; b) A. Curcio, A. K. Silva, S. Cabana, A. Espinosa, B. Baptiste, N. Menguy, C. Wilhelm, A. Abou-Hassan, *Theranostics* **2019**, *9*, 1288.
[44] a) E. Cazares-Cortes, A. Espinosa, J.-M. Guigner, A. Michel, N. Griffete, C. Wilhelm, C. Ménager, *ACS Appl. Mater. Inter.* **2017**, *9*, 25775; b) N. Griffete, J. Fresnais, A. Espinosa, C. Wilhelm, A. Bee, C. Menager, *Nanoscale* **2015**, DOI: 10.1039/C5NR06133D.
[45] S. Wilhelm, A. J. Tavares, Q. Dai, S. Ohta, J. Audet, H. F. Dvorak, W. C. Chan, *Nature Reviews Materials* **2016**, *1*, 16014.
[46] Q. Dai, S. Wilhelm, D. Ding, A. M. Syed, S. Sindhwani, Y. Zhang, Y. Y. Chen, P. MacMillan, W. C. Chan, *ACS nano* **2018**, *12*, 8423.
[47] K. Jiang, D. A. Smith, A. Pinchuk, *The Journal of Physical Chemistry C* **2013**, *117*, 27073.
[48] a) P. B. Johnson, R.-W. Christy, *Physical review B* **1972**, *6*, 4370; b) M. Querry, *US Army Chemical Research, Development and Engineering Center (CRDC), Aberdeen Proving Ground, MD* **1985**, *418*.

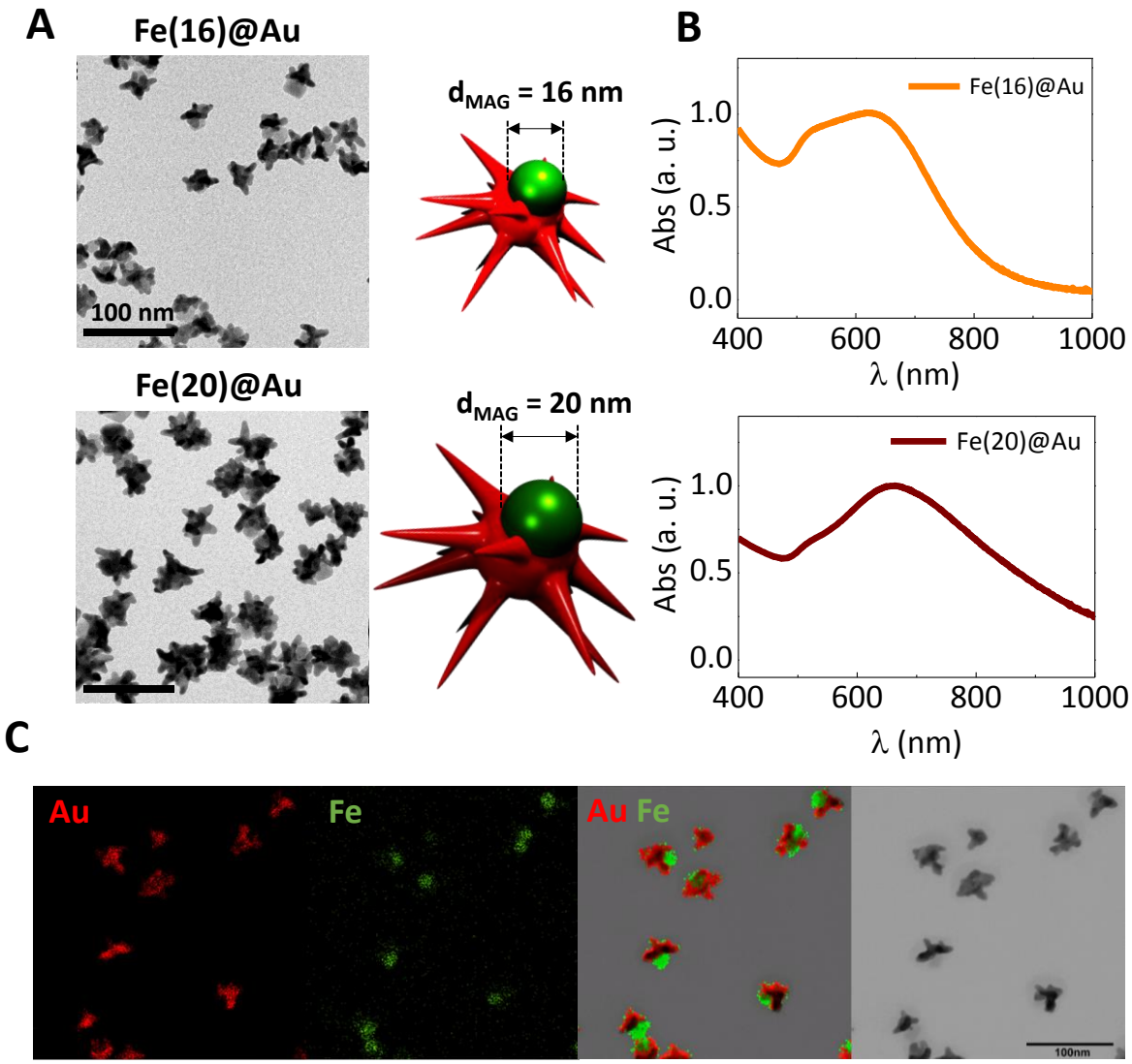

Figure 1. Janus gold-iron oxide nanoparticles with tunable gold branched-shell and iron oxide core. (**A)** Transmission electron micrographs of Janus nanoparticles with different morphologies and gold nanostar sizes: (upper panel) 16-nm iron oxide core nanoparticles, Fe(16)@Au (average total diameter of 28.5 nm) and (lower panel) 20-nm iron oxide core nanoparticles, Fe(20)@Au (average total diameter of 35.8 nm, respectively). (**B)** UV-Vis-NIR spectra of the previous set of samples. (**C**) EDX Au elemental map (red), EDX Fe elemental map (green), overlaid elemental maps and bright field micrograph of Fe(16)@Au nanoparticles.

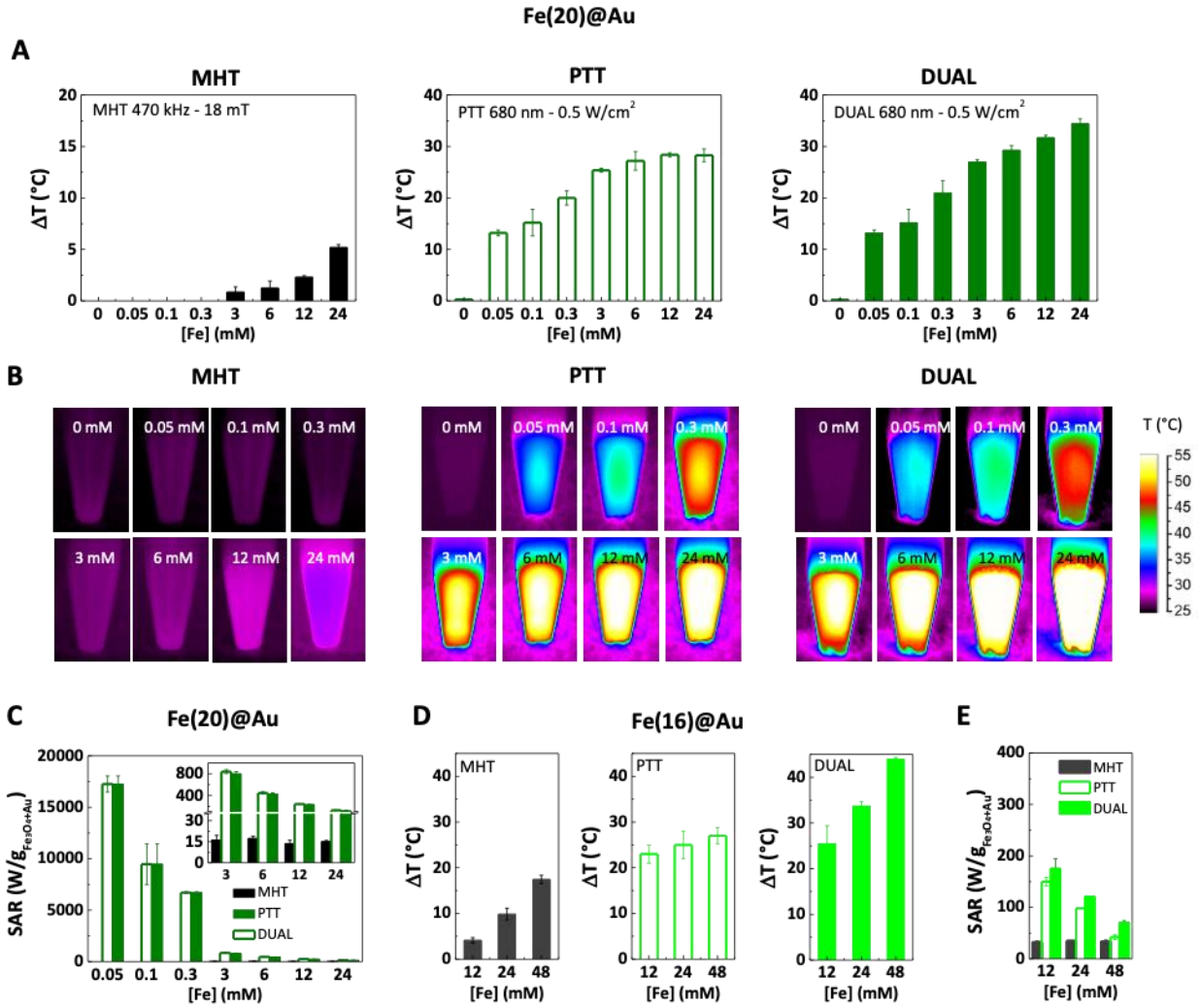

Figure 2. Heating properties of gold-iron oxide nanoparticles in aqueous dispersion. (**A**) Temperature increment plots of Fe(20)@Au nanoparticles (molecular ration Au/Fe = 2.3) subjected to 5 min of magnetic hyperthermia (MHT, 470 kHz and 18 mT), 680 nm-laser photothermia (PTT, 0.5 W/cm^2) and both treatments simultaneously (DUAL) at different concentrations in Fe (in the 0.05-24 mM range). (**B**) Corresponding panel of thermal images acquired by the IR camera for Fe(20)@Au nanoparticles suspension, after 5 min of MHT, PTT and DUAL protocols. (**C**) Heating capacity of previous samples under the three thermal protocols (in W per mass of material ($m_{Fe3O4+Au}$)). (**D**) Temperature increase of Fe(16)@Au nanoparticles at high Fe concentration (12-48 mM, Au/Fe = 1.6), after 5 min of each treatment (MHT, PTT and DUAL). (**E**) Heating capacities of Fe(16)@Au nanoparticles.

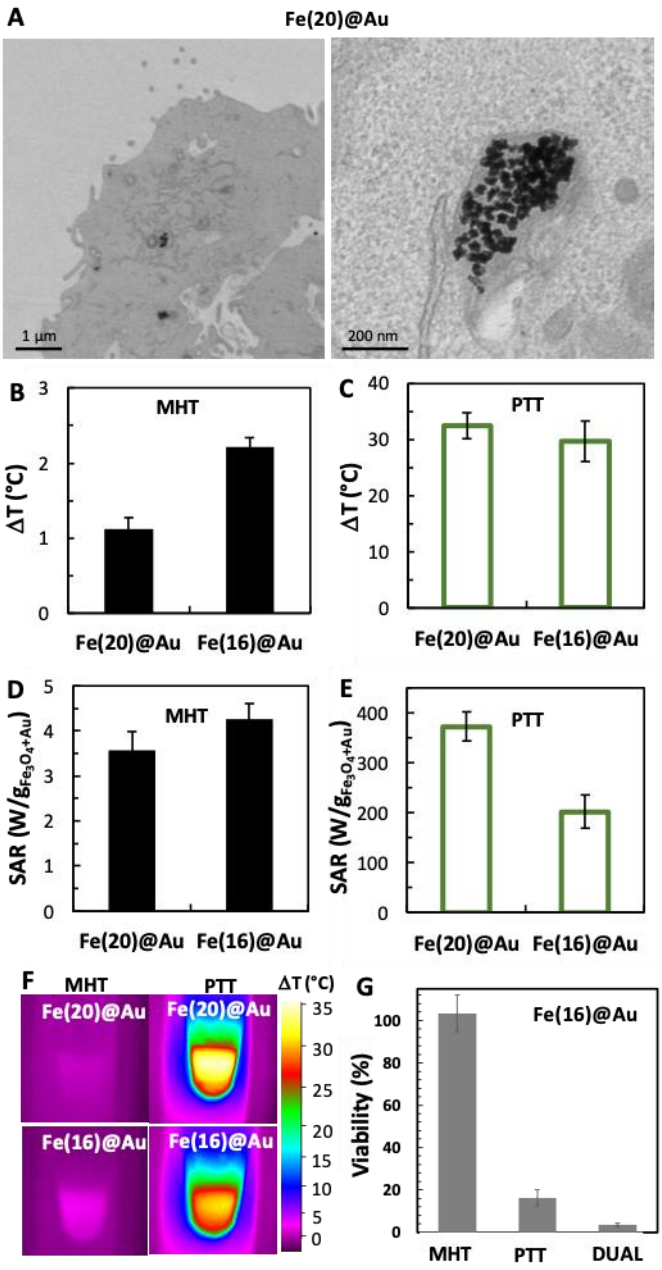

Figure 3. Heating properties of Janus gold-iron oxide in the cellular environment. CT-26 cancer cells were incubated with Janus nanoparticles (Fe(20)@Au or Fe(16)@Au) at incubation iron concentration $[Fe]_{inc}$ = 100 µM for 24 hours. (**A**) TEM of Fe(20)@Au after cell incubation show all nanoparticles clearly localized within the cells, densely confined inside intracellular endosomes. All cells contain endosomes-loaded nanoparticles (**B-G**) Upon incubation, cell pellets were formed, to reach a global iron concentration of [Fe] = 6 mM (see Table 1 for corresponding cell density in the pellet), and further exposed to magnetic hyperthermia (MHT, 470 kHz and 18 mT) or illuminated with a laser (PTT, 680 nm and 0.5 W/cm²) for 5 minutes. **(B-C)** Average temperature elevations reached by MHT (B) or PTT (C). **(D-E)** SAR values of the cells pellets similarly exposed to MHT (D) or PTT (E). **(F)** Typical infrared thermal images of the cell pellets containing Fe(20)@Au (top) and Fe(15)@Au (bottom) exposed to MHT (left) or PTT (right). **(G)** Viability of CT-26 cells incubated with Fe(16)@Au under MHT, PTT and DUAL (MHT+PTT).

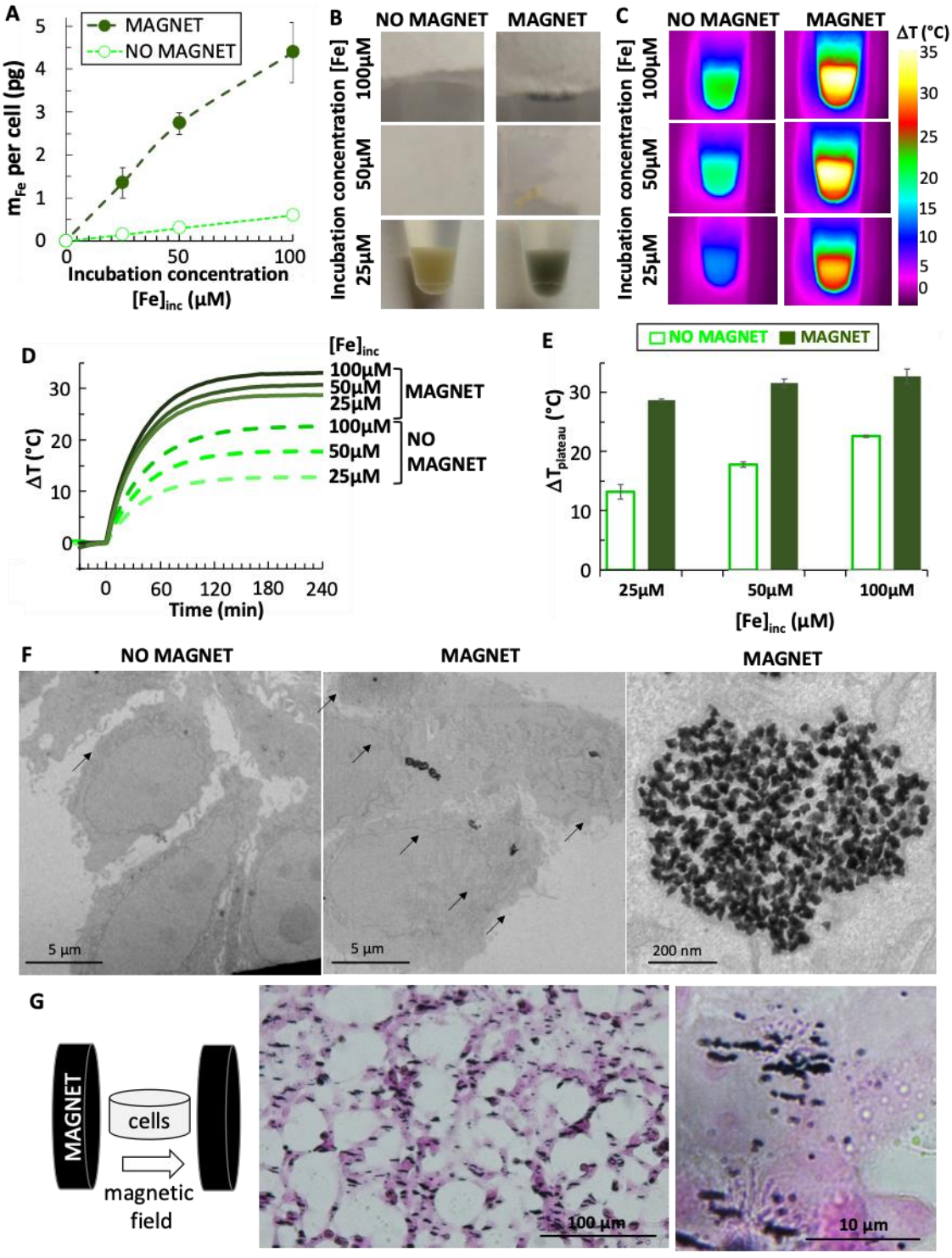

Figure 4. Magnetic guiding-assisted photothermia of Janus gold-iron oxide *(in vitro)*. (**A**) Magnetic guiding effect was evaluated placing a permanent magnet (B = 0.2 T, grad B = 50 T/m) below the culture dishes (MAGNET conditions) and compared with standard culture conditions (NO MAGNET). The cells where incubated with Fe(20)@Au for 3 h at the extracellular concentrations of [Fe] = 25, 50 and 100 µM, then 3 million cells were resuspended in 50 µL (see Table 1 for resulting iron concentrations of the cellular pellets). (**A**) Mass of iron measured by magnetophoresis of nanoparticles internalized in cells at both incubation conditions. The mass values were retrieved by monitoring the magnetic attraction of single cells

toward a magnet (B = 0.14 T, grad B = 17 T/m). (**B**) Camera images of cell pellets under different incubation conditions. The dark color is linked to the high dosage of iron and gold load in the cell pellets. (**C**) Infrared thermal images, (**D**) typical heating curves and (**E**) average plateau temperature elevation of cell pellets illuminated with laser (680 nm-laser 0.5 W/cm²) after 5 min, for all conditions. (**F**) TEM images of CT-26 cells incubated with nanoparticles. A significant increase of cellular uptake of nanoparticles is observed under magnet application. (**G**) External magnetic field application along the cell incubation plane (scheme). Prussian blue staining of cells fixed after 1 hour of magnetic field application, where formation of magnetic chains of endosomes in the cell tissue are observed.

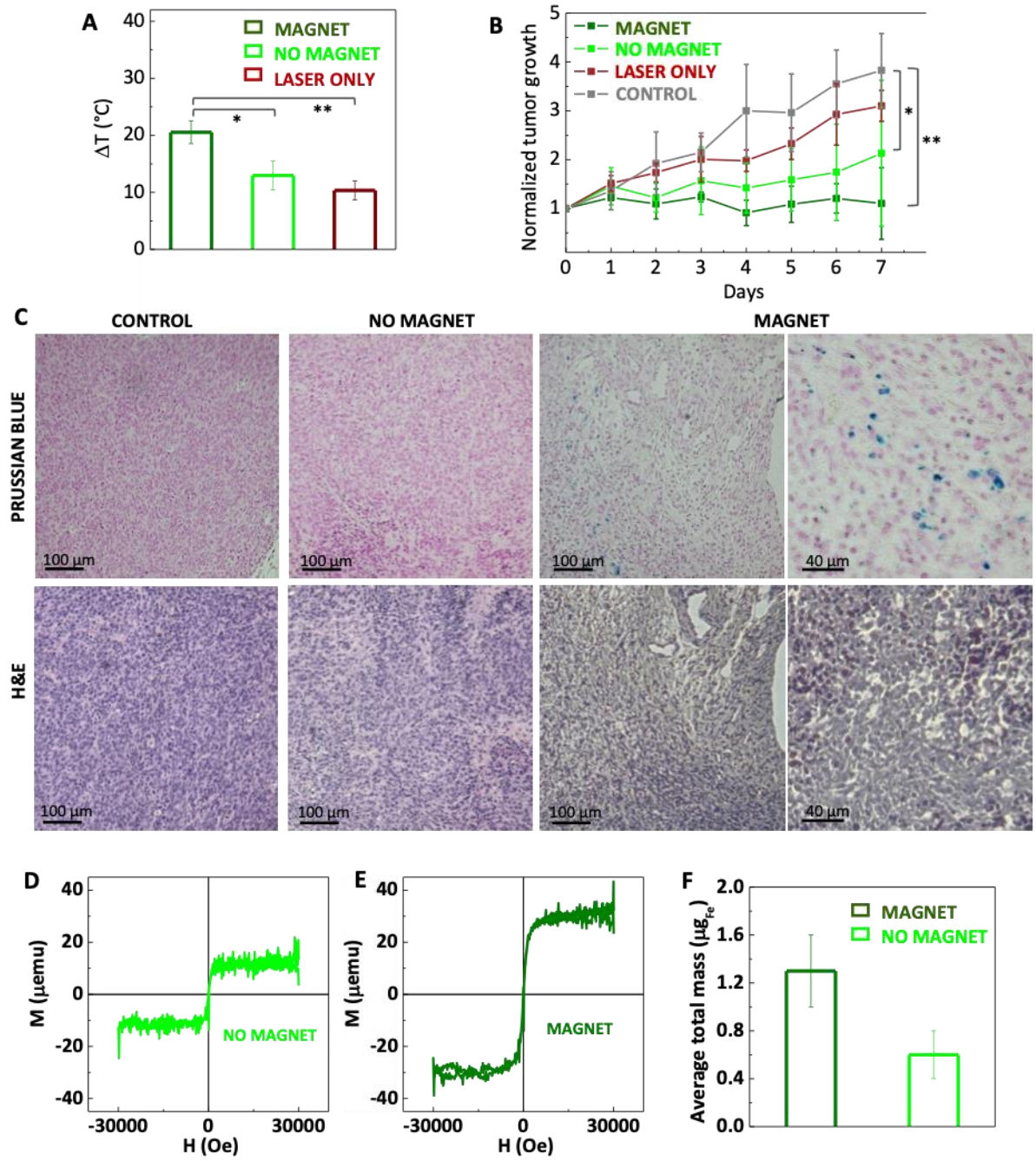

Figure 5. Magnetically guided photothermal effect in tumors *(in vivo)*. (**A**) Temperature increment of CT-26 tumor-bearing mice after intravenous injection of Fe(16)@Au nanoparticles and exposed to 680 nm laser (0.8 W/cm^2) for 15 min with the assistance of magnetic field guidance (MAGNET), without magnetic field (NO MAGNET). Temperature increase of non-injected control tumors was also monitored (LASER ONLY). Non-injected and non-treated tumors served as CONTROLS. (**B**) Tumor growth from mice after the different treatments. (**C**) Prussian blue and hematoxylin–eosin (H&E) stained tumor sections from mice with different treatments. Magnetic hysteresis loops measured at 300 K (in µemu) of tumors after intravenous injection of nanoparticles (**D**) without the assistance of magnetic field guidance (NO MAGNET) and (**E**) with (MAGNET). (**D**) Average total mass of iron (in µg) of accumulated nanoparticles in tumors at both conditions.

Nanoparticles	$[Fe]_{inc}$ (mM)	t_{inc} (h)	mag	mFe (pg_{Fe}/cell)	cell sample density (million/mL)	$[Fe]_{cell\ sample}$ (mM)	ΔT (°C) MHT	ΔT (°C) PTT
Fe(16)@Au	0.1	24	no	2.9 ± 0.5	116	6	2.2 ± 0.1	29.7 ± 3.6
Fe(16)@Au	0.1	24	no	2.9 ± 0.5	58	3	1.2 ± 0.4	30 ± 1.6
Fe(16)@Au	0.02	24	no	0.8 ± 0.2	106	1.5	0.6 ± 0.2	25 ± 4
Fe(20)@Au	0.1	24	no	3.1 ± 0.6	108	6	1.1 ± 0.15	32.3 ± 2.3
Fe(20)@Au	0.1	3	no	0.6 ± 0.1	60	0.6	-	22.5 ± 1.1
Fe(20)@Au	0.05	3	no	0.29 ± 0.04	60	0.3	-	17.8 ± 0.9
Fe(20)@Au	0.025	3	no	0.15 ± 0.1	60	0.15	-	13.2 ± 1.2
Fe(20)@Au	0.1	3	yes	4.4 ± 0.7	60	4.7	-	32.7 ± 1.2
Fe(20)@Au	0.05	3	yes	2.7 ± 0.25	60	3	-	31.5 ± 1.4
Fe(20)@Au	0.025	3	yes	1.35 ± 0.35	60	1.4	-	28.6 ± 1.5

Table 1: Uptake of the nanoparticles in cells, at extracellular concentration of [Fe] = 100 µM, for different incubation times (t_{inc}), with or without the application of a magnet (mag). Mass of iron per cell (m_{Fe}, expressed in pg_{Fe} per cell). Heating (ΔT, expressed in °C) of the cellular samples (final concentration for the cells suspension $[Fe]_{cell\ sample}$), upon magnetic hyperthermia (MHT) or photothermia (PTT). Note that the cells pellets contain about 2.5 or 5 million cells in 50 µL (cell density in the range of 50 or 100 million cells per mL, respectively).

Supporting Information

Janus Magnetic-Plasmonic Nanoparticles for Magnetically Guided and Thermally Activated Cancer Therapy

Tables and Figures

Nano-materials	Structure type	Environ-ment	[Fe] (mM)	[Au] or [Ag] (mM)	H_{AC} (mT) MHT	f (kHz) MHT	Power irradiation (W/cm^2) PTT	λ (nm) PTT	Time (s)	Heating ΔT (°C) MHT + PTT	Ref.
Fe_3O_4@Au	Core-shell	In solution	7.0	7.9-37.2	25	900	0.3	680	300	9-19	[15a]
Fe_3O_4@Ag	Core-shell	In solution	18	6	10-80	310	0.5-0.9	442	300	10-50	[15b]
Fe_3O_4@Au	Core-shell	In solution	7	2.3	6.2	560	0.3	800	300	22	[15c]
Fe_3O_4@Au	Janus	In solution	0.05-48	0.06-62.4	18	470	0.5	680	300	13-44	Present work

Table S1. Magneto-plasmonic nanostructures for combined MHT and PTT based on gold (or silver) and iron oxide including different nanostructures configurations (core-shell and Janus), nanoparticle concentration, MHT and PTT experimental parameters (alternating magnetic field amplitude (H_{AC}), frequency (f), power irradiation and wavelength (λ)), time of application and temperature elevation ΔT.

Nano-materials	Structure type	Environment	Administra-tion	Material injected (mg)	Power irradiation (W/cm^2) PTT	λ (nm) PTT	Time (s)	Heating ΔT (°C)	Ref.
Drug loaded Au@Fe@Au	Muti-shell	In vivo	I.v.	0.15	1.3	808	600 (2 days)	45	[14a]
Drug loaded Au@Fe_3O_4	Core-mesoporous shell	In vivo	I.v.	0.2	1.0	808	420 (1 day)	47, 57 (magnet)	[18a]
Polymer modified Au@Fe_3O_4	Core-mesoporous shell	In vivo	I.v.	0.15	2.0	808	180 (10 days)	67 (magnet)	[18c]
Fe_3O_4@Au	Janus	In vivo	I.v.	0.5	0.8	680	900 (1 day)	20 (magnet)	Present work

Table S2. Magneto-plasmonic nanostructures for *in vivo* magnetic-guided PTT based on gold and iron oxide including different nanostructures configurations (multi-shell, core-shell and Janus), administration type, mass of injected material, PTT experimental parameters (power irradiation and wavelength (λ)), time of treatment and temperature elevation ΔT.

Sample	Iron oxide diameter (nm)	Initial gold seed diameter (nm)	Average total diameter	[Au]/[Fe]	M_S (emu/g_{Fe})
Fe(16)@Au	16.2 ± 2.8	5.3 ± 0.8	28.5 ± 2.9	1.6	74 ± 3
Fe(20)@Au	20.5 ± 4.0	5.7 ± 1.2	35.8 ± 5.0	2.3	77 ± 4

Table S3: Structural and magnetization characteristics of Fe(16)@Au and Fe(20)@Au NPs: iron oxide diameter (nm), gold diameter (nm), average total size (nm), gold/iron molar ratio and saturation magnetization (emu/g_{Fe}).

Sample	Bond	R (Å)	N	σ^2
Fe(16)@Au	Au-Au	2.86(1)	11(1)	0.0089(5)
Fe(20)@Au	Au-Au	2.85(1)	11(1)	0.0086(5)
Au metal foil	Au-Au	2.85(1)	12(1)	0.0085(5)

Table S4: Fitting structural parameters of the Au shell obtained from experimental EXAFS results of Janus nanoparticles and Au foil reference at the Au L-edge. R is the interatomic Au-Au distance, N is the coordination number and σ^2 is the Debye-Waller (DW) factor. The amplitude reduction factor S_0^2 was fixed to 0.9, according to the fitting results of the Au bulk data to the structural model. The on-structural parameter, E_0, was constrained in a range of +/- 2 eV respect to that obtained in the bulk, which was 5(1) eV. All the other parameters were kept free during each fitting.

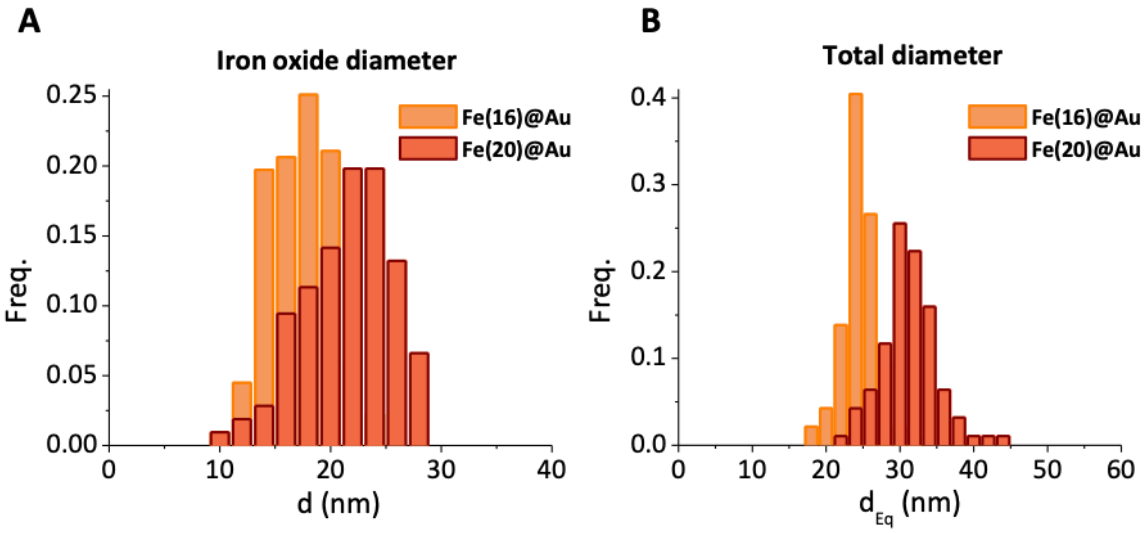

Figure S1. Size distribution histograms of Fe(16)@Au and Fe(20)@Au NPs obtained from TEM measurements of (**A**) iron oxide diameter (magnetite) and **(B**) average equivalent total diameter (to a sphere) of the whole nanoparticle.

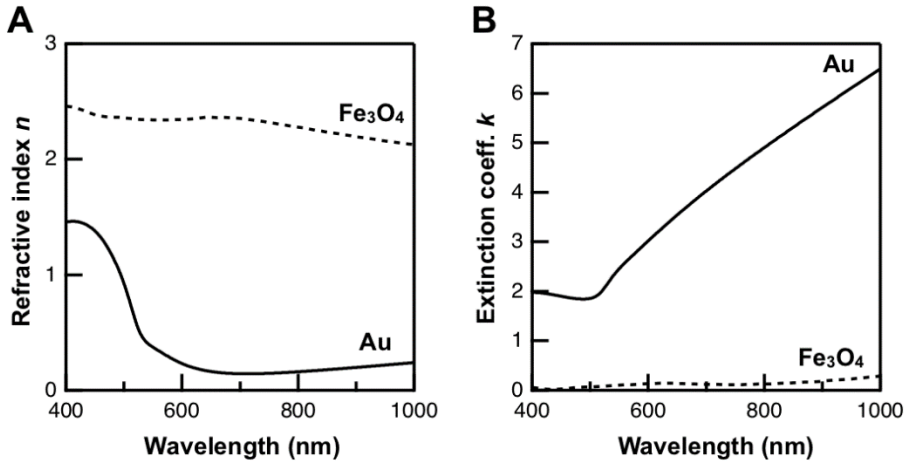

Figure S2. Optical properties used for the FDTD simulations: (**A**) refractive index *n* and (**B**) mass attenuation coefficient *k* of Au (solid line) and Fe_3O_4 (dashed line). The complex refractive index was defined as $n + ik$.

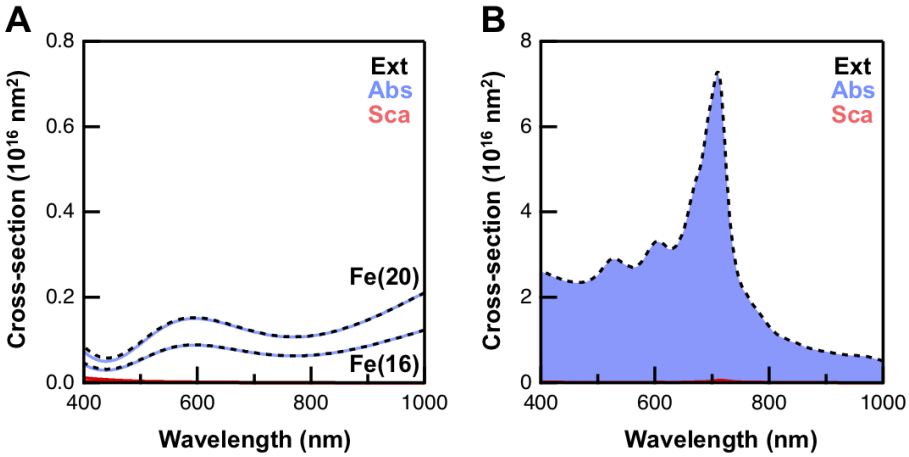

Figure S3. Extinction (black, dashed), absorption (blue), and scattering (red) cross-sections as calculated by FDTD numerical modelling: (**A**) Fe_3O_4 nanospheres of 16 nm and 20 nm in diameter, showing minute scattering contributions below 500 nm. (**B**) Fe(20)@Au Janus nanoparticles, averaged over 16 morphologies and orientations to the excitation plane. The nanoparticles are dominantly absorbing throughout the entire spectral range**,** with a minor scattering contribution at the plasmon peak wavelength.

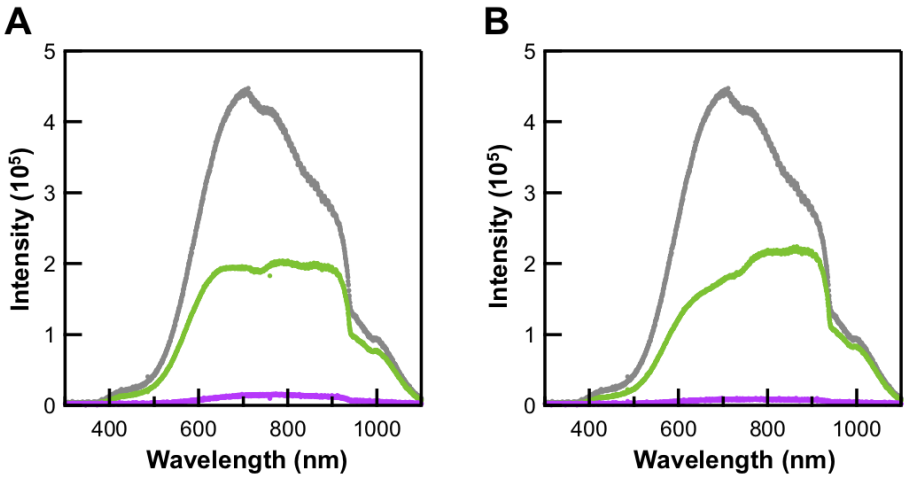

Figure S4. Characterization of spectral losses by diffuse reflectance spectroscopy of (**A**) Fe(16)@Au and (**B**) Fe(20)@Au nanoparticles: raw transmittance spectra of nanoparticle dispersions without (green) and with light trap (violet); for both samples, the transmittance spectrum of water, measured without light trap, served as a reference (gray).

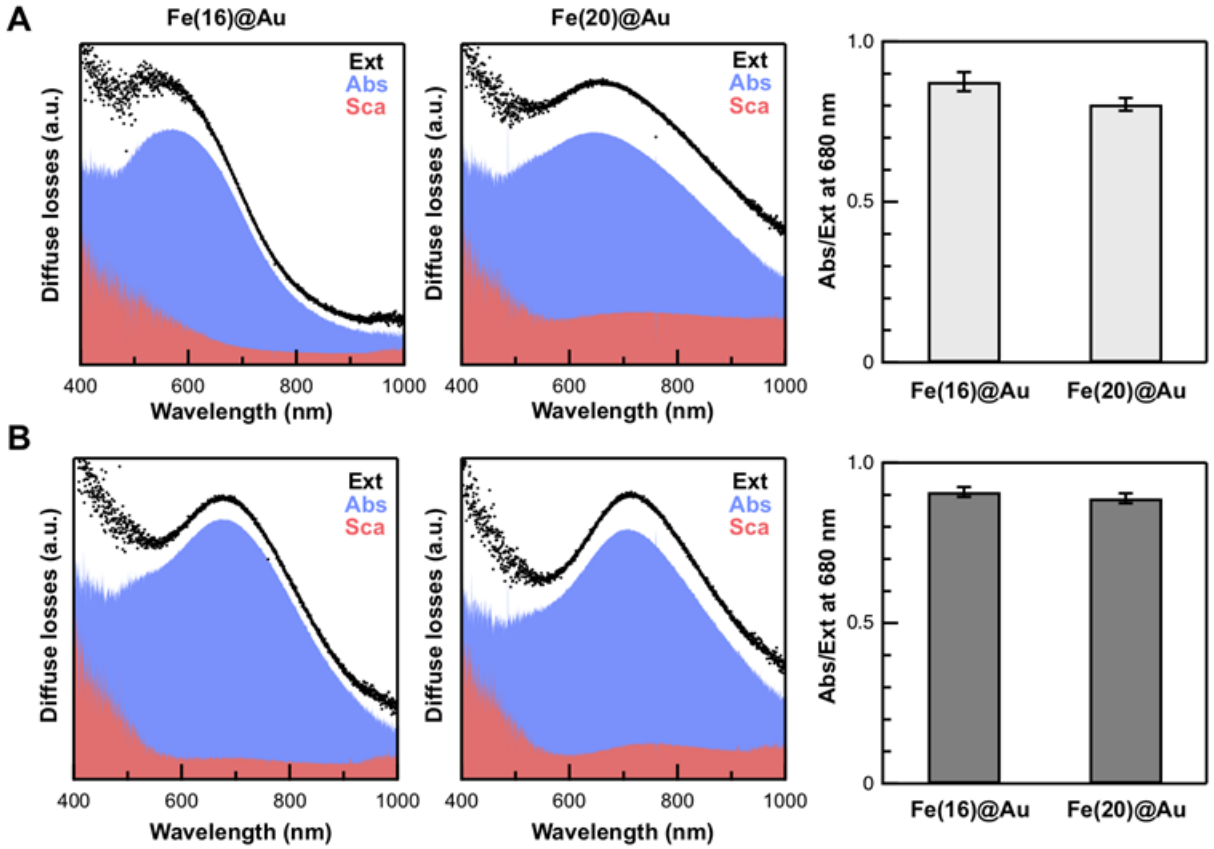

Figure S5. Spectral losses measured by diffuse reflectance spectroscopy of Fe(16)@Au and Fe(20)@Au dispersions, showing contributions from absorption (blue) and scattering (red) to the total extinction (black) for samples after a storage time of 48 months (**A**) and freshly prepared samples (**B**). The experimental absorption/extinction ratios at 680 nm indicate the radiative losses due to diffuse light scattering. Owing to reshaping, the scattering losses of older samples increased from below 12% up to 19%. Please note that the pronounced data scattering, visible below 550 nm and above 950 nm, is not noise but reflects the sensitivity profile of the detector under low light conditions (c. f. Figure S4).

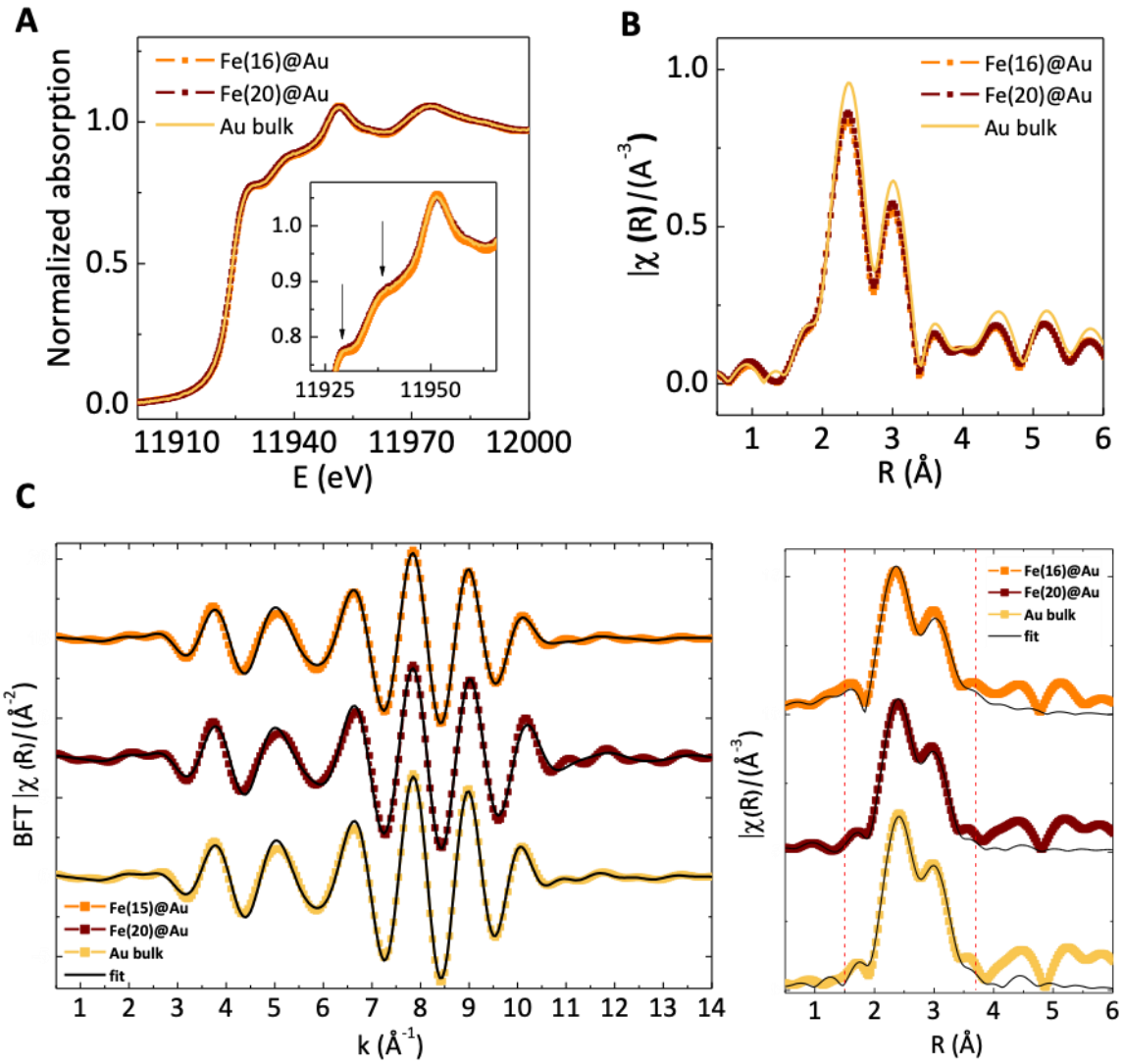

Figure S6. (**A**) X-ray absorption measurements: XANES (X-ray absorption near-edge structure, left) and (**B**) EXAFS (X-ray absorption fine structure, right) spectra at the Au-L_3 edge of Fe(16)@Au and Fe(20)@Au samples compared with Au metallic bulk. (**C**) EXAFS filtered signal and EXAFS fitting results for the Fourier transform of previous samples.

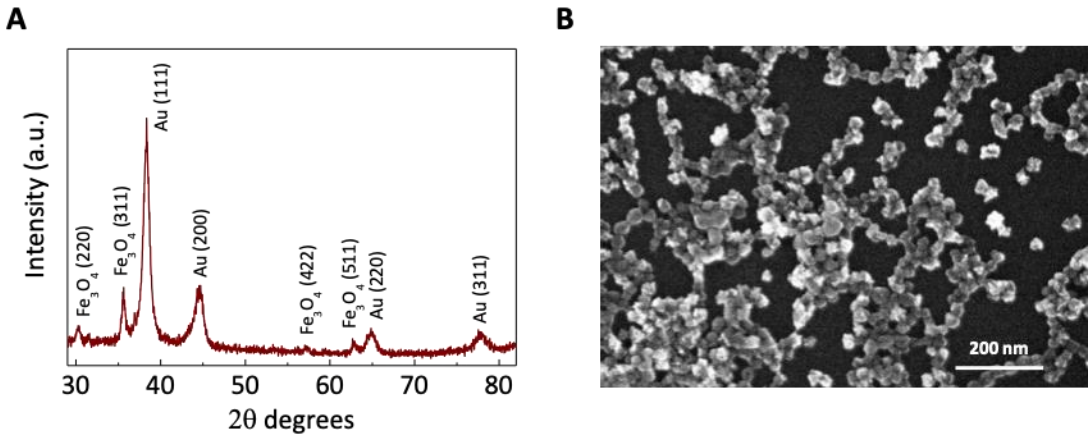

Figure S7. (**A**) X-ray diffraction pattern and (**B**) scanning electron microscopy (SEM) image of Fe(20)@Au nanoparticles. Scale bar: 200 nm

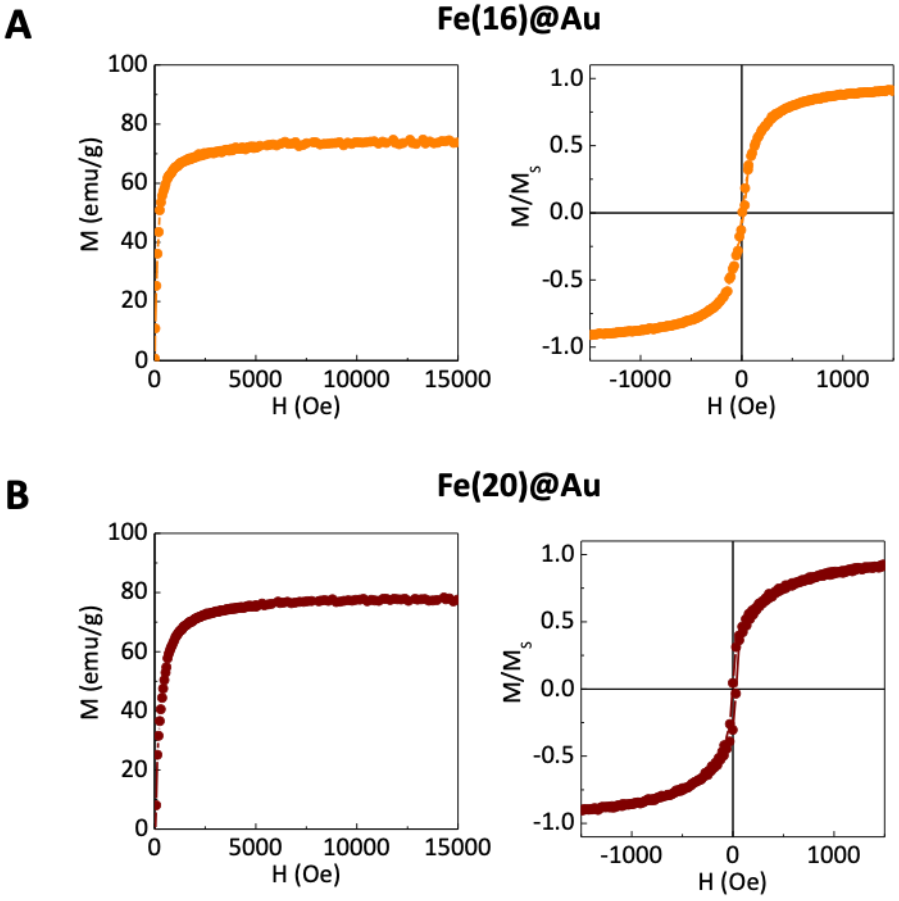

Figure S8. Magnetization curves at 300 K of (**A**) Fe(16)@Au and (**B**) Fe(20)@Au nanoparticles in solution. Left panels show a detail of the normalized magnetization at low-field region (-1500 - 1500 Oe).

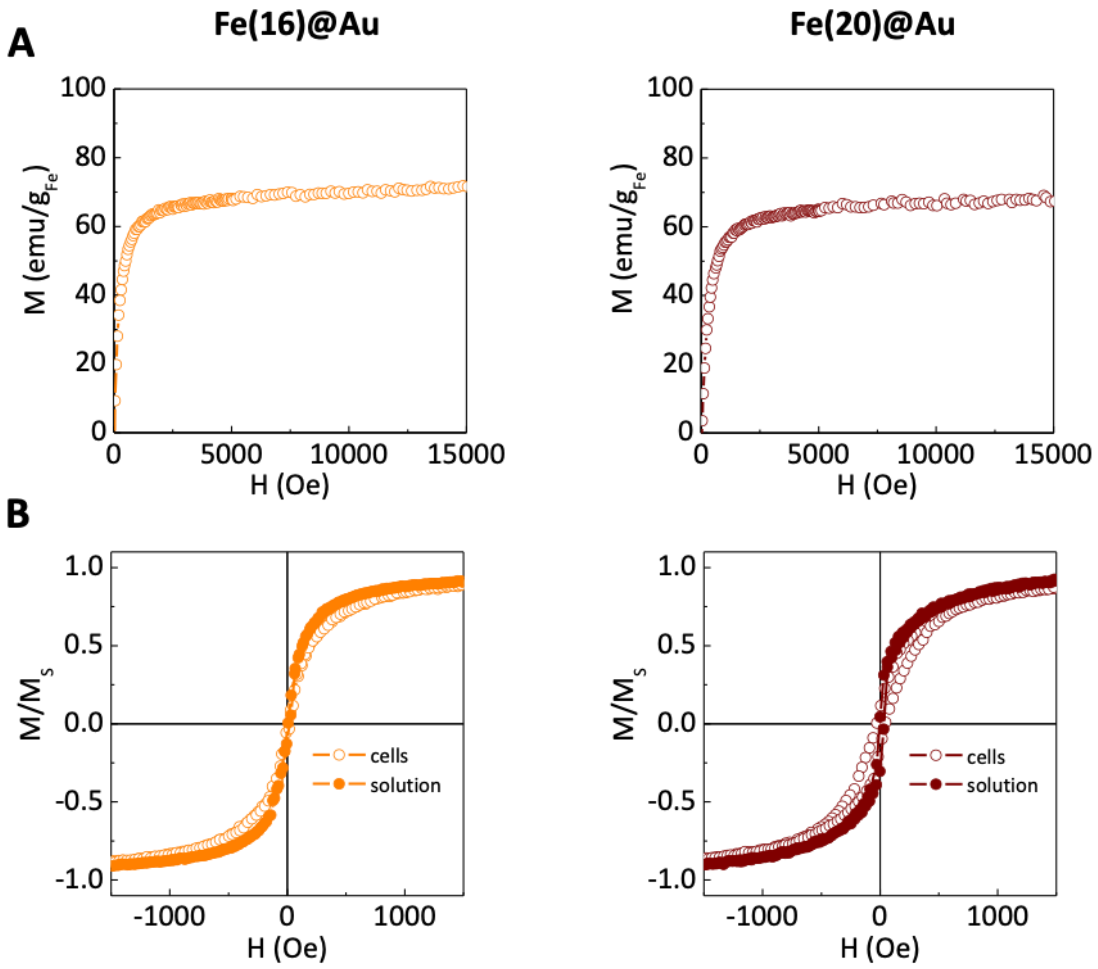

Figure S9. (**A**) Magnetization curves at 300 K of Fe(16)@Au and Fe(20)@Au nanoparticles in cells. (**B**) Comparison of normalized magnetization curves of both nanoparticles in solution and inside cells at low-field region (-1500 - 1500 Oe).